Imaginary-time open-chain path-integral approach for two-state time correlation functions and applications in charge transfer

Cite as: J. Chem. Phys. 157, 114111 (2022); https://doi.org/10.1063/5.0098162

Submitted: 05 May 2022 • Accepted: 16 August 2022 • Accepted Manuscript Online: 16 August 2022 • Published Online: 21 September 2022









ARTICLES YOU MAY BE INTERESTED IN

Renormalization of excitonic properties by polar phonons

The Journal of Chemical Physics 157, 104116 (2022); https://doi.org/10.1063/5.0100738

Quantum dynamics using path integral coarse-graining

The Journal of Chemical Physics 157, 181102 (2022); https://doi.org/10.1063/5.0120386

Computing chemical potentials of solutions from structure factors

The Journal of Chemical Physics 157, 121101 (2022); https://doi.org/10.1063/5.0107059





Imaginary-time open-chain path-integral approach for two-state time correlation functions and applications in charge transfer

Cite as: J. Chem. Phys. 157, 114111 (2022); doi: 10.1063/5.0098162 Submitted: 5 May 2022 • Accepted: 16 August 2022 • Published Online: 21 September 2022









Zengkui Liu, 1,2,3 D Wen Xu, 1,2 Mark E. Tuckerman, 2,3,4,a D and Xiang Sun 1,2,3,5,b D







AFFILIATIONS

- Division of Arts and Sciences, NYU Shanghai, 1555 Century Avenue, Shanghai 200122, China
- ²NYU-ECNU Center for Computational Chemistry at NYU Shanghai, 3663 Zhongshan Road North, Shanghai 200062, China
- Department of Chemistry, New York University, New York, New York 10003, USA
- Courant Institute of Mathematical Sciences, New York University, New York, New York 10012, USA
- ⁵State Key Laboratory of Precision Spectroscopy, East China Normal University, Shanghai 200062, China
- ^{a)}Electronic mail: mark.tuckerman@nyu.edu
- b) Author to whom correspondence should be addressed: xiang.sun@nyu.edu

ABSTRACT

Quantum time correlation functions (TCFs) involving two states are important for describing nonadiabatic dynamical processes such as charge transfer (CT). Based on a previous single-state method, we propose an imaginary-time open-chain path-integral (OCPI) approach for evaluating the two-state symmetrized TCFs. Expressing the forward and backward propagation on different electronic potential energy surfaces as a complex-time path integral, we then transform the path variables to average and difference variables such that the integration over the difference variables up to the second order can be performed analytically. The resulting expression for the symmetrized TCF is equivalent to sampling the open-chain configurations in an effective potential that corresponds to the average surface. Using importance sampling over the extended OCPI space via open path-integral molecular dynamics, we tested the resulting path-integral approximation by calculating the Fermi's golden rule CT rate constant within a widely used spin-boson model. Comparing with the real-time linearized semiclassical method and analytical result, we show that the imaginary-time OCPI provides an accurate two-state symmetrized TCF and rate constant in the typical turnover region. It is shown that the first bead of the open chain corresponds to physical zerotime and that the endpoint bead corresponds to final time t; oscillations of the end-to-end distance perfectly match the nuclear mode frequency. The two-state OCPI scheme is seen to capture the tested model's electronic quantum coherence and nuclear quantum effects accurately.

Published under an exclusive license by AIP Publishing. https://doi.org/10.1063/5.0098162

I. INTRODUCTION

A central theme in quantum dynamics is the calculation of quantum time correlation functions (TCFs), which describe numerous dynamical phenomena such as chemical reaction rates, transport properties, spectroscopic line shapes, and neutron and light scattering. Generally, the standard quantum TCF of the operators \hat{A} at time 0 and \hat{B} at time t for the system described by Hamiltonian \hat{H} is given by

$$C(t) = \langle \hat{A}(0)\hat{B}(t)\rangle = \frac{1}{Z} \mathrm{Tr}_N \left[e^{-\beta \hat{H}} \hat{A} e^{i\hat{H}t/\hbar} \hat{B} e^{-i\hat{H}t/\hbar} \right], \tag{1}$$

where $Tr_N[\cdot]$ is the trace over the (nuclear) Hilbert space, $Z = \text{Tr}_N[e^{-\beta \hat{H}}]$ is the canonical partition function, and $\beta = 1/k_B T$ is the inverse temperature (k_B is the Boltzmann's constant and \hbar is the reduced Planck's constant). Such TCFs incorporate (nuclear) quantum effects such as tunneling effect and zero-point energy, which can be significant when the system includes light nuclear particles, such as hydrogen, or is at low temperatures.^{2,3} For small molecular systems, if the potential energy surface is known, the most accurate way of obtaining TCFs is arguably through direct time evolution of the wavefunction from the time-dependent Schrödinger equation. 4-7 However, the computational overhead of wavefunction methods is prohibitively high for complex or condensed-phase systems with many degrees of freedom (DOFs). Thus, it is desirable to have more practical dynamical methods that can be used to treat large systems.

The last half century has witnessed numerous efforts in developing approximate approaches for evaluating TCFs of large systems. One such approach is the semiclassical initial value representation (SC-IVR) proposed by Miller^{8–10} and its forward–backward version proposed by Makri, ^{11–13} where the time evolution of a quantum system is transformed into a trajectory problem that is more tractable than wavefunction methods. More practical schemes are based on a linearization approximation that leads to the linearized semiclassical (LSC)^{14–16} or equivalent classical Wigner model,¹⁷ which can be derived directly from the linearization of the forward–backward real-time path integrals as shown by Shi and Geva. ^{18–20} Consequently, LSC is also called the linearized path integral (LPI) approach. ^{21–25}

Alternatively, Feynman path-integral techniques have become a popular choice for incorporating nuclear quantum effects in thermodynamic or time-independent properties in condensed phases.²⁶⁻²⁹ By partitioning the quantum Boltzmann operator $\exp(-\beta \hat{H})$ into P slices or "beads," one can construct a representation of the quantum-mechanical equilibrium distribution that is isomorphic to classical ring-polymers consisting of P beads as $P \rightarrow \infty$.³⁰ The exact quantum mechanical statistics can be obtained by sampling the extended ring-polymer configuration space, using, e.g., path-integral Monte Carlo (PIMC)³¹ or path-integral molecular dynamics (PIMD). Since $\exp(-\beta \hat{H})$ can be considered as a quantum propagator $\exp(-i\hat{H}t/\hbar)$ in imaginary time $t = -i\beta\hbar$, PIMC and PIMD are commonly referred to as imaginary-time pathintegral approaches. The advantage of imaginary-time methods is that the distribution is positive-definite and, therefore, ensemble averages converge rapidly, as there are no highly oscillatory quantum phase factors as occur in the real-time propagator. Such factors typically cause convergence issues in real-time path-integral methods such as LSC/LPI.

Imaginary-time methods have become widely used to approximate quantum TCFs under the assumption that PIMD with physical masses captures some dynamical information. This class of methods includes centroid molecular dynamics (CMD)³⁶ and ring-polymer molecular dynamics (RPMD),³⁷ both of which have recently been shown to be limiting cases of the numerically "exact" Matsubara dynamics.³⁸ Taking advantage of the cyclic symmetry of the ring-polymers, CMD and RPMD directly generate the Kubo-transformed TCF. Recently, we showed how RPMD could be applied to the simulation of two-dimensional vibrational spectroscopy in liquids to incorporate nuclear quantum effects via the double Kubo-transformed correlation functions.³⁹ However, due to the fact that CMD/RPMD lacks quantum phase factors, the applicability of these imaginary-time path-integral based dynamical schemes needs to be carefully considered before they are generally applied.

A new approach to include quantum phase information is to combine imaginary-time path-integral techniques with a second-order expansion in the variables that describe difference between forward- and backward-time paths. Recently, Robertson and Habershon⁴⁰ and Cendagorta *et al.*⁴¹ independently proposed the open-chain path-integral (OCPI) approach for obtaining the symmetrized TCF defined as

$$G(t) = \frac{1}{7} \text{Tr}_N \Big[\hat{A} e^{i\hat{H}\tau_c^*/\hbar} \hat{B} e^{-i\hat{H}\tau_c/\hbar} \Big], \tag{2}$$

where τ_c is a complex time parameter given by $\tau_c = t - i\beta\hbar/2$. It can be shown that the standard quantum TCF and the symmetrized version are related through their Fourier transforms, ⁴²

$$\tilde{C}(\omega) = e^{\beta\hbar\omega/2}\tilde{G}(\omega). \tag{3}$$

The idea is similar to real-time LSC/LPI for symmetrized $TCF^{43,44}$ except that it can be formulated as an imaginary-time sampling approach as follows: We start from the complex-time forward and backward propagators in the symmetrized TCF, transform the bead position variables into averages and differences of the complextime paths, and truncate an expansion of the potential in the forward-backward path integrals at second order in the path difference variables. When this is done, a positive-definite imaginary-time OCPI sampling scheme is obtained that can provide quantum phase information up to second order in the forward-backward path differences. This imaginary-time sampling approach can be evaluated by any numerical sampling scheme, for example, molecular dynamics, 41 Monte Carlo, 40 or enhanced sampling methods. 45 It is important to note that the method can be systematically improved by including higher-order terms to yield a numerically formally "exact" approach, 41 although beyond second order, the integrals over the path difference variables can no longer be performed analytically.

The situation becomes more complicated when considering nonadiabatic transitions between different electronic states. For example, Fermi's golden rule (FGR) charge transfer (CT) rate constant for donor-to-acceptor transition requires a quantum TCF involving two electronic states, 46,47

$$C_{AD}(t) = \frac{1}{Z_D} \text{Tr}_N \left[e^{-\beta \hat{H}_D} \hat{A} e^{i\hat{H}_A t/\hbar} \hat{B} e^{-i\hat{H}_D t/\hbar} \right], \tag{4}$$

where $\hat{H}_{D/A}$ denote the donor/acceptor-state nuclear Hamiltonians and $Z_D = \text{Tr}_N [e^{-\beta \hat{H}_D}]$ is the donor-state partition function. The fundamental difference between the single-state TCF in Eq. (1) and two-state TCF in Eq. (4) is that the Heisenberg-picture operand two-state 101 in Eq. (1) is a self-term and two-state 101 in Eq. (1) has a well-defined classical limit, whereas $e^{i\hat{H}_At/\hbar}\hat{B}e^{-i\hat{H}_Dt/\hbar}$ in Eq. (4) corresponds to quantum coherence and, thus, does not have a well-defined classical limit.⁴⁶ Beyond the single-state contribution, the energy gap between two electronic states also contributes to the highly oscillatory quantum phase factor, which is considerably more difficult to compute. For this reason, conventional mixed quantum-classical dynamical methods without explicit treatment of the electronic decoherence, such as fewest-switches surface hopping (FSSH)⁴⁸ and Ehrenfest dynamics, 49 can deviate significantly from exact quantum mechanical FGR rate constants. Thus, it is essential to develop dynamical methods that can capture electronic decoherence in a consistent manner.

In this work, we extend the OCPI approach⁴¹ to two-state symmetrized quantum TCFs and show this sampling scheme is able to capture approximate quantum phase information explicitly. We start by constructing the two-state symmetrized quantum TCF for FGR CT rate constant. Next, we express the complex-time forward

and backward path integrals and transform the bead variables evolving on two electronic potential energy surfaces to path average and difference variables, and we truncate the Taylor expansion of the forward and backward path-integral actions at second order in the difference variables. As with the real-time LSC/LPI method, the effective Hamiltonian and corresponding Boltzmann distribution can be written as the average surface between the donor and acceptor states, but the Hamiltonian becomes complex. We propose to use importance sampling to harvest the open-chain configurations using the real OCPI effective Hamiltonian corresponding to the average surface. We test this algorithm using a widely applied benchmark spin-boson model for condensed-phase CT processes, 50-52 where the exact quantum mechanical expression of FGR is known in closed form.46 We will also compare the newly developed imaginary-time OCPI scheme against the traditional real-time LSC/LPI approach⁴⁶ in numerical accuracy. Furthermore, we investigate structures and energy contributions of the open chains since an effective sampling of the open-chain configurations has a decisive influence on the accuracy of OCPI calculations.

The remainder of this paper is organized as follows: In Sec. II, we derive the open-chain path-integral formalism for two-state symmetrized TCFs and show its relation with the TCFs required in the Fermi's golden rule rate constant. The benchmark spin-boson model Hamiltonian is described in Sec. III. Computational techniques are described in Sec. IV. Results are reported and discussed in Sec. V. Concluding remarks are provided in Sec. VI. The proof of the relation between the two-state symmetrized TCF and the standard TCF is shown in the Appendix.

II. THEORY

We begin by briefly outlining the FGR CT rate constant given by time integration of the two-state quantum TCF and its LSC/LPI expression. Then, we derive the OCPI expressions for the corresponding two-state symmetrized TCF.

A. Fermi's golden rule charge transfer rate constant

We consider a two-state Hamiltonian for modeling CT process between diabatic donor and acceptor electronic states, i.e., $|D\rangle$ and $|A\rangle$, respectively,

$$\hat{H} = \hat{H}_D |D\rangle\langle D| + \hat{H}_A |A\rangle\langle A| + \hat{\Gamma}_{DA} |D\rangle\langle A| + \hat{\Gamma}_{AD} |A\rangle\langle D|. \tag{5}$$

Here, $\hat{H}_{D/A}$ are the corresponding nuclear Hamiltonians,

$$\hat{H}_{D/A} = \frac{\hat{\mathbf{p}}^2}{2} + V_{D/A}(\hat{\mathbf{R}}), \tag{6}$$

where $\hat{\mathbf{R}} = (\hat{R}_1, \dots, \hat{R}_N)$ and $\hat{\mathbf{P}} = (\hat{P}_1, \dots, \hat{P}_N)$ are the mass-weight nuclear position operators and their conjugate momentum operators, respectively, $V_{D/A}(\hat{\mathbf{R}})$ are potential energy surfaces (PESs) for the corresponding states, and N is the number of nuclear DOFs. $\hat{\Gamma}_{DA}$ and $\hat{\Gamma}_{AD}$ represent the electronic coupling between the donor and acceptor states, and within the Condon approximation, they are assumed to be constant, i.e., $\hat{\Gamma}_{DA} = \hat{\Gamma}_{AD}^{\dagger} = \Gamma$.

The FGR rate constant for nonadiabatic electronic transitions can be obtained via second-order time-dependent perturbation

theory by treating $\hat{H}_0 = \hat{H}_D |D\rangle\langle D| + \hat{H}_A |A\rangle\langle A|$ as the unperturbed Hamiltonian and the electronic coupling $\hat{H}_I = \hat{\Gamma}_{DA} |D\rangle\langle A| + \hat{\Gamma}_{AD} |A\rangle\langle D|$ as the perturbation. As in the equilibrium FGR formalism,⁵³ the system is assumed to start out at thermal equilibrium in the donor state, i.e., $\hat{\rho}(0) = \hat{\rho}_D^{\rm eq} |D\rangle\langle D|$ and $\hat{\rho}_D^{\rm eq} = \frac{1}{Z_D} e^{-\beta \hat{H}_D}$, where Z_D is the donor-state partition function. The FGR CT rate constant for $D \to A$ electronic transition is given by

$$k = \frac{2}{\hbar^2} \text{Re} \int_0^\infty dt \ C_{DA}(t) = \frac{1}{\hbar^2} \int_{-\infty}^\infty dt \ C_{DA}(t),$$
 (7)

where the quantum time correlation function involves propagators on two different electronic states, $C_{DA}(t)$, is derived from the off-diagonal electronic coupling autocorrelation function,

$$C_{DA}(t) = \operatorname{Tr}_{N} \operatorname{Tr}_{e} \left[\hat{\rho}(0) e^{i\hat{H}_{0}t/\hbar} \hat{H}_{I} e^{-i\hat{H}_{0}t/\hbar} \hat{H}_{I} \right]$$

$$= \frac{1}{Z_{D}} \operatorname{Tr}_{N} \left[e^{-\beta \hat{H}_{D}} e^{i\hat{H}_{D}t/\hbar} \hat{\Gamma}_{DA} e^{-i\hat{H}_{A}t/\hbar} \hat{\Gamma}_{AD} \right]. \tag{8}$$

Here, $\operatorname{Tr}_e[\cdot]$ denotes trace over the electronic Hilbert space. In Eq. (7), we can also use $C_{AD}(t)$ [Eq. (4)] in the integrand, i.e.,

$$C_{AD}(t) = \frac{1}{Z_D} \operatorname{Tr}_N \left[e^{-\beta \hat{H}_D} \hat{\Gamma}_{DA} e^{i\hat{H}_A t/\hbar} \hat{\Gamma}_{AD} e^{-i\hat{H}_D t/\hbar} \right], \tag{9}$$

since $C_{AD}(t) = C_{DA}^*(t)$, which can be shown using $\hat{\Gamma}_{DA} = \hat{\Gamma}_{AD}^{\dagger}$ and cyclic invariance of trace, $\text{Tr}[\hat{A}\hat{B}\hat{C}] = \text{Tr}[\hat{C}\hat{A}\hat{B}] = \text{Tr}[\hat{B}\hat{C}\hat{A}]$.

Note that the validity of using a rate constant to describe CT is based on the separation of timescales, where the decay time of $C_{DA}(t)$ is much faster than k^{-1} . Otherwise, one would have to consider transient effects that give rise to a time-dependent rate coefficient, which can be addressed by the nonequilibrium FGR. ^{54–57}

B. The real-time linearized semiclassical (linearized path-integral) scheme

The LSC/LPI approximation for the two-state quantum TCF is obtained by casting $C_{DA}(t)$ in a real-time path-integral form and truncating the expansion of the forward–backward action in terms of the path difference variables at first order. The resulting LSC/LPI expression for $C_{DA}(t)$ is given by^{20,46,47}

$$C_{DA}^{LSC/LPI}(t) = \int d\mathbf{R}_0 d\mathbf{P}_0 \left[\hat{\Gamma}_{AD} \hat{\rho}_D^{\text{eq}} \right]_W (\mathbf{R}_0, \mathbf{P}_0)$$

$$\times \left[\hat{\Gamma}_{DA} \right]_W (\mathbf{R}_t^{\text{av}}, \mathbf{P}_t^{\text{av}}) \exp \left[-\frac{i}{\hbar} \int_0^t \Delta V(\mathbf{R}_\tau^{\text{av}}) d\tau \right], \quad (10)$$

where $\Delta V(\mathbf{R}) = V_A(\mathbf{R}) - V_D(\mathbf{R})$ is the energy gap between the acceptor and donor states, and the Wigner transform of any operator \hat{A} is defined as

$$\left[\hat{A}\right]_{W}(\mathbf{R}, \mathbf{P}) = \int d\mathbf{Z} e^{-i\mathbf{Z}\cdot\mathbf{P}/\hbar} \left\langle \mathbf{R} + \frac{\mathbf{Z}}{2} \left| \hat{A} \right| \mathbf{R} - \frac{\mathbf{Z}}{2} \right\rangle. \tag{11}$$

In the LSC/LPI prescription, $(\mathbf{R}_t^{av}, \mathbf{P}_t^{av})$ are obtained from classical trajectories starting from initial conditions $(\mathbf{R}_0, \mathbf{P}_0)$ sampled

from the Wigner distribution and propagating up to time t on the average PES,

$$\overline{V}(\mathbf{R}) = \frac{1}{2} [V_D(\mathbf{R}) + V_A(\mathbf{R})]. \tag{12}$$

The real-time fluctuations in the energy gap contribute to the quantum phase factor $\exp\left[-\frac{i}{\hbar}\int_0^t \Delta V(\mathbf{R}_{\tau}^{av})d\tau\right]$, which is difficult to converge due to its highly oscillatory behavior.

C. Open-chain path-integral scheme for two-state symmetrized TCF

We now develop the OCPI formulation for the two-state symmetrized TCF. We start out by introducing the corresponding symmetrized TCF that corresponds to the $C_{AD}(t)$ in Eq. (9) by replacing t with $t + i\beta\hbar/2$,

$$G_{AD}(t) = \frac{1}{Z_D} \operatorname{Tr}_N \left[\hat{\Gamma}_{DA} e^{it\hat{H}_A \tau_c^*/\hbar} \hat{\Gamma}_{AD} e^{-it\hat{H}_D \tau_c/\hbar} \right], \tag{13}$$

where τ_c is the complex time $\tau_c = t - i\beta\hbar/2$. As in the single-state case [Eq. (3)], it can be shown that the two-state standard and symmetrized TCFs are related through their Fourier transforms (see the Appendix for proof),

$$\tilde{C}_{AD}(\omega) = e^{\beta\hbar\omega/2} \tilde{G}_{AD}(\omega). \tag{14}$$

For simplicity, in this section, we restrict ourselves to one-dimensional nuclear-space notation, i.e., $\hat{H}_{D/A} = \hat{p}^2/(2m) + V_{D/A}(\hat{x})$, and we assume that the electronic coupling operators $\hat{\Gamma}_{DA}$, $\hat{\Gamma}_{AD}$ are functions of the nuclear position \hat{x} only. Expressing the trace in Eq. (13) in the position basis, we have

$$G_{AD}(t) = \int dx dx' \Gamma_{DA}(x) \langle x | e^{i\hat{H}_A \tau_c^*/\hbar} | x' \rangle \Gamma_{AD}(x') \langle x' | e^{-i\hat{H}_D \tau_c/\hbar} | x \rangle,$$
(15)

where $\Gamma_{DA}(x)$ and $\Gamma_{AD}(x')$ are eigenvalues of the operator $\hat{\Gamma}_{DA}$ at position x and the operator $\hat{\Gamma}_{AD}$ at position x', respectively, $\left\langle x' \middle| e^{-i\hat{H}_D\tau_c/\hbar}\middle| x \right\rangle$ is the forward complex-time quantum propagator from x to x', and $\left\langle x \middle| e^{i\hat{H}_A\tau_c^*/\hbar}\middle| x' \right\rangle$ is the backward complex-time quantum propagator from x to x'. We slice the forward and backward propagators into P beads each (for a total of 2P beads) by inserting 2P closure relations and obtain the discretized path-integral expression for $G_{AD}(t)$,

$$G_{AD}(t) = \frac{1}{Z_D} \int dx^{(1)} \cdots dx^{(2P)} \Gamma_{DA}(x^{(1)}) \Gamma_{AD}(x^{(P+1)})$$

$$\times \prod_{\alpha=1}^{P} \left\langle x^{(\alpha+1)} \Big| e^{-i\hat{H}_D \varepsilon/\hbar} \Big| x^{(\alpha)} \right\rangle \prod_{\alpha=P+1}^{2P} \left\langle x^{(\alpha+1)} \Big| e^{i\hat{H}_A \varepsilon^*/\hbar} \Big| x^{(\alpha)} \right\rangle,$$
(16)

where $\varepsilon = \tau_c/P$ denotes the complex time segment, $\mathbf{x} = (x^{(1)}, \dots, x^{(2P)})$ denote the bead positions, and the trace requires a closed ring-polymer boundary condition $x^{(2P+1)} = x^{(1)}$. Applying a Trotter

splitting for each short-time propagator as below, ^{29,30,41}

$$\left\langle x^{(\alpha+1)} \middle| e^{-i\hat{H}_{D}\varepsilon/\hbar} \middle| x^{(\alpha)} \right\rangle \approx \sqrt{\frac{m}{2\pi i\hbar\varepsilon}} \exp\left\{ \frac{i}{\hbar} \frac{m}{2\varepsilon} \left(x^{(\alpha+1)} - x^{(\alpha)} \right)^{2} - \frac{i}{\hbar} \varepsilon \left[\frac{V_{D}(x^{(\alpha+1)}) + V_{D}(x^{(\alpha)})}{2} \right] \right\}, \quad (17)$$

$$\left\langle x^{(\alpha+1)} \middle| e^{i\hat{H}_A \varepsilon^* / \hbar} \middle| x^{(\alpha)} \right\rangle \approx \sqrt{\frac{m}{-2\pi i \hbar \varepsilon^*}} \exp \left\{ -\frac{i}{\hbar} \frac{m}{2\varepsilon^*} \left(x^{(\alpha+1)} - x^{(\alpha)} \right)^2 + \frac{i}{\hbar} \varepsilon^* \left[\frac{V_A(x^{(\alpha+1)}) + V_A(x^{(\alpha)})}{2} \right] \right\}, (18)$$

we obtain an exact quantum mechanical path-integral expression for the two-state symmetrized TCF,

$$G_{AD}(t) = \frac{1}{Z_D} \int d\mathbf{x} \, \Gamma_{DA}(x^{(1)}) \Gamma_{AD}(x^{(P+1)}) \rho(\mathbf{x}) e^{i\phi(\mathbf{x})}.$$
 (19)

Here, $\rho(\mathbf{x})$ is a positive-definite distribution given by

$$\rho(\mathbf{x}) = \left(\frac{mP}{2\pi\hbar|\tau_c|}\right)^P \exp\left\{-\sum_{\alpha=1}^{2P} \left[A\left(x^{(\alpha+1)} - x^{(\alpha)}\right)^2 + \frac{\beta}{2P}V_D(x^{(\alpha)})\right] - \frac{\beta}{2P}\Delta V_{RP}(\mathbf{x})\right\}\Big|_{\mathbf{x}^{(2P+1)} = \mathbf{x}^{(1)}}, \tag{20}$$

the phase factor $\phi(\mathbf{x})$ is given by

$$\phi(\mathbf{x}) = \frac{\gamma}{2} \left[\sum_{\alpha=1}^{P} \left(x^{(\alpha+1)} - x^{(\alpha)} \right)^2 - \sum_{\alpha=P+1}^{2P} \left(x^{(\alpha+1)} - x^{(\alpha)} \right)^2 \right] - \frac{t}{P\hbar} \left[\sum_{\alpha=2}^{P} V_D(x^{(\alpha)}) - \sum_{\alpha=P+2}^{2P} V_D(x^{(\alpha)}) \right] + \frac{t}{P\hbar} \Delta V_{RP}(\mathbf{x}).$$
 (21)

Here, for simplicity, we denote

$$A = \frac{mP\beta}{4|\tau_c|^2}, \qquad \gamma = \frac{mPt}{\hbar|\tau_c|^2}, \tag{22}$$

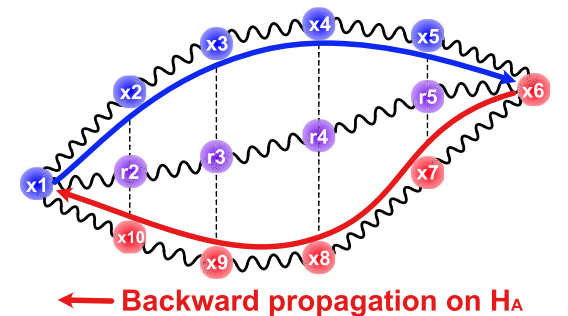
and

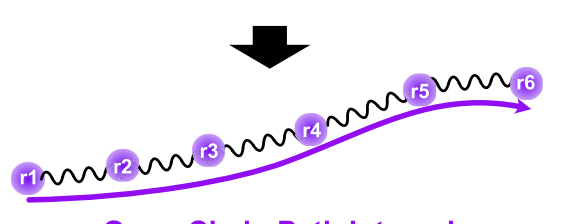
$$\Delta V_{RP}(\mathbf{x}) = \frac{1}{2} \Delta V(x^{(1)}) + \frac{1}{2} \Delta V(x^{(P+1)}) + \sum_{\alpha=P+2}^{2P} \Delta V(x^{(\alpha)}), \quad (23)$$

where $\Delta V(x) = V_A(x) - V_D(x)$ is the energy gap between donor and acceptor states. The phase factor ϕ in Eq. (21) still exists even if $\Delta V = 0$, and we refer to this phase contribution as the nuclear quantum coherence, in contrast with the electronic quantum coherence for which $\Delta V \neq 0$.

Next, as illustrated in Fig. 1, we introduce an open-chain path-integral approximation to Eq. (19). First, we define the path average and difference variables, $\mathbf{r} = (r^{(1)}, \dots, r^{(P+1)})$ and $\mathbf{s} = (s^{(2)}, \dots, s^{(P)})$, respectively, as follows:⁴¹

Forward propagation on H_D →





Open-Chain Path Integral

FIG. 1. Schematic representation of the open-chain path-integral transformation [Eq. (24)]. A closed ring polymer of 2P beads (P=5 shown here) including P beads of forward propagation on \hat{H}_D (blue) and P beads of backward propagation on \hat{H}_A (red) is transformed into an open chain of P+1 path-integral beads (purple). The vertical dashed lines indicate the same physical times increasing from left to right, and the open-chain beads are the averages between the corresponding forward-path and backward-path beads.

$$r^{(1)} = x^{(1)},$$

$$r^{(P+1)} = x^{(P+1)},$$

$$r^{(\alpha)} = \frac{1}{2} \left[x^{(\alpha)} + x^{(2P+2-\alpha)} \right] \quad (\alpha = 2, \dots, P),$$

$$s^{(\alpha)} = x^{(\alpha)} - x^{(2P+2-\alpha)} \quad (\alpha = 2, \dots, P).$$
(24)

The inverse transformation from ${\bf r}$ and ${\bf s}$ back to the bead positions ${\bf x}$ is

$$x^{(1)} = r^{(1)},$$

$$x^{(P+1)} = r^{(P+1)},$$

$$x^{(\alpha)} = r^{(\alpha)} + \frac{1}{2}s^{(\alpha)} \quad (\alpha = 2, ..., P),$$

$$x^{(2P+2-\alpha)} = r^{(\alpha)} - \frac{1}{2}s^{(\alpha)} \quad (\alpha = 2, ..., P).$$
(25)

Second, we rewrite the distribution function ρ [Eq. (20)] and the phase factor ϕ [Eq. (21)] in terms of \mathbf{r} and \mathbf{s} and expand the potential energies about $s^{(\alpha)} = 0$ up to second order; for $\alpha = 2, \ldots, P$, we obtain

$$V_{D}(x^{(\alpha)}) = V_{D}\left(r^{(\alpha)} + \frac{1}{2}s^{(\alpha)}\right)$$

$$\approx V_{D}(r^{(\alpha)}) + \frac{1}{2}V'_{D}(r^{(\alpha)})s^{(\alpha)} + \frac{1}{8}V''_{D}(r^{(\alpha)})(s^{(\alpha)})^{2},$$

$$(26)$$

$$V_{D}(x^{(2P+2-\alpha)}) = V_{D}\left(r^{(\alpha)} - \frac{1}{2}s^{(\alpha)}\right)$$

$$\approx V_{D}(r^{(\alpha)}) - \frac{1}{2}V'_{D}(r^{(\alpha)})s^{(\alpha)} + \frac{1}{8}V''_{D}(r^{(\alpha)})(s^{(\alpha)})^{2}.$$

The potential energy terms in the distribution function ρ become

$$\sum_{\alpha=1}^{2P} V_D(x^{(\alpha)}) \approx V_D(r^{(1)}) + V_D(r^{(P+1)}) + 2\sum_{\alpha=2}^{P} \left[V_D(r^{(\alpha)}) + \frac{1}{8} V_D''(r^{(\alpha)}) (s^{(\alpha)})^2 \right], \quad (27)$$

and the potential energy terms in the phase factor ϕ become

$$\sum_{\alpha=2}^{P} V_{D}(x^{(\alpha)}) - \sum_{\alpha=P+2}^{2P} V_{D}(x^{(\alpha)}) \approx \sum_{\alpha=2}^{P} V'_{D}(r^{(\alpha)}) s^{(\alpha)}, \qquad (28)$$

$$\sum_{\alpha=P+2}^{2P} \Delta V(x^{(\alpha)}) = \sum_{\alpha=2+P}^{2P} \Delta V\left(r^{(\alpha)} - \frac{1}{2}s^{(\alpha)}\right)$$

$$\approx \sum_{\alpha=P+2}^{2P} \Delta V(r^{(\alpha)}) - \frac{1}{2}\Delta V'(r^{(\alpha)}) s^{(\alpha)}$$

$$+ \frac{1}{6}\Delta V''(r^{(\alpha)}) (s^{(\alpha)})^{2}. \qquad (29)$$

Third, collecting terms in the distribution and phase factor as a function of average and difference variables (\mathbf{r}, \mathbf{s}) , denoting the inbetween average variables $\mathbf{r}' = (r^{(2)}, \dots, r^{(P)})$, and calling the average PES $\overline{V}(x) = \frac{1}{2} [V_A(x) + V_D(x)]$, we obtain the OCPI distribution and phase factor expressions as follows:

$$\rho(\mathbf{r}, \mathbf{s}) = \rho_{1}(\mathbf{r}) \rho_{2}(\mathbf{r}', \mathbf{s}), \tag{30}$$

$$\rho_{1}(\mathbf{r}) = \left(\frac{mP}{2\pi\hbar|\tau_{c}|}\right)^{P} \exp\left\{-A\left[2\sum_{\alpha=1}^{P}\left(r^{(\alpha+1)} - r^{(\alpha)}\right)^{2}\right] - \frac{\beta}{2P}\left[\overline{V}(r^{(1)}) + \overline{V}(r^{(P+1)}) + 2\sum_{\alpha=2}^{P}\overline{V}(r^{(\alpha)})\right]\right\}, \tag{31}$$

$$\rho_{2}(\mathbf{r}', \mathbf{s}) = \exp\left\{-\frac{A}{2}\left[\sum_{\alpha=2}^{P-1}\left(s^{(\alpha+1)} - s^{(\alpha)}\right)^{2} + \left(s^{(2)}\right)^{2} + \left(s^{(P)}\right)^{2}\right] - \frac{\beta}{2P}\sum_{\alpha=2}^{P}\left[-\frac{1}{2}\overline{V}'(r^{(\alpha)})s^{(\alpha)} + \frac{1}{4}\overline{V}''(r^{(\alpha)})(s^{(\alpha)})^{2}\right]\right\}, \tag{32}$$

$$\phi(\mathbf{r}) = \gamma\sum_{\alpha=2}^{P}\left(2r^{(\alpha)} - r^{(\alpha-1)} - r^{(\alpha+1)}\right)s^{(\alpha)} - \frac{t}{P\hbar}\sum_{\alpha=2}^{P}\overline{V}'(r^{(\alpha)})s^{(\alpha)} + \frac{t}{P\hbar}\left[\sum_{\alpha=2}^{P}\Delta V(r^{(\alpha)}) + \frac{1}{2}\Delta V(r^{(1)}) + \frac{1}{2}\Delta V(r^{(P+1)}) + \sum_{\alpha=2}^{P}\frac{1}{8}\Delta V''(r^{(\alpha)})(s^{(\alpha)})^{2}\right]. \tag{33}$$

Fourth, we define a tridiagonal $(P-1) \times (P-1)$ matrix $\mathbf{M}(\mathbf{r}')$ with elements

$$M_{\alpha\alpha'}(\mathbf{r}') = \left[2A + \frac{\beta}{4P}\overline{V}''(r^{(\alpha)}) - \frac{it}{4P\hbar}\Delta V''(r^{(\alpha)})\right]\delta_{\alpha\alpha'} - A\delta_{\alpha+1,\alpha'} - A\delta_{\alpha,\alpha'+1} \quad (\alpha, \alpha' = 2, \dots, P),$$
(34)

(P-1)-dimensional vector $\mathbf{K}(\mathbf{r})$ with components

$$K_{\alpha}(\mathbf{r}) = \gamma \left(2r^{(\alpha)} - r^{(\alpha-1)} - r^{(\alpha+1)}\right) - \frac{t}{P\hbar} \overline{V}'(r^{(\alpha)})$$
$$-\frac{i\beta}{4P} \Delta V'(r^{(\alpha)}) \quad (\alpha = 2, \dots, P), \tag{35}$$

and the phase factor Φ due to electronic quantum coherence as

$$\Phi(\mathbf{r}) = \frac{t}{P\hbar} \left[\sum_{\alpha=2}^{P} \Delta V(r^{(\alpha)}) + \frac{1}{2} \Delta V(r^{(1)}) + \frac{1}{2} \Delta V(r^{(P+1)}) \right].$$
(36)

The two-state symmetrized TCF in Eq. (19) can then be expressed as

$$G_{AD}(t) = \frac{1}{Z_D} \int d\mathbf{r} \rho_1(\mathbf{r}) \Gamma_{DA}(r^{(1)}) \Gamma_{AD}(r^{(P+1)}) e^{i\Phi(\mathbf{r})}$$

$$\times \int d\mathbf{s} \ e^{-\frac{1}{2}\mathbf{s}^T \mathbf{M}(\mathbf{r}')\mathbf{s} + i\mathbf{K}(\mathbf{r})\mathbf{s}}.$$
(37)

The integration over the path difference variables s in Eq. (37) is a multivariate Gaussian integral, which can be evaluated analytically via

$$\int d\mathbf{s} \ e^{-\frac{1}{2}\mathbf{s}^T \mathbf{M}(\mathbf{r}')\mathbf{s} + i\mathbf{K}(\mathbf{r})\mathbf{s}} = \sqrt{\frac{(2\pi)^{P-1}}{\det[\mathbf{M}(\mathbf{r}')]}} e^{-\frac{1}{2}\mathbf{K}(\mathbf{r})^T \mathbf{M}^{-1}(\mathbf{r}')\mathbf{K}(\mathbf{r})}. \quad (38)$$

Finally, inserting Eq. (38) into Eq. (37), we obtain the main result of this paper, i.e., the open-chain path-integral formula for the two-state symmetrized TCF or two-state open path symmetrized correlation function (OPSCF),

$$G_{AD}(t) = \frac{(2\pi)^{(P-1)/2}}{Z_D} \int d\mathbf{r} \rho_1(\mathbf{r}) \Gamma_{DA}(r^{(1)}) \Gamma_{AD}(r^{(P+1)}) e^{i\Phi(\mathbf{r})}$$
$$\times e^{-\frac{1}{2} \left[\mathbf{K}(\mathbf{r})^T \mathbf{M}^{-1}(\mathbf{r}') \mathbf{K}(\mathbf{r}) + \ln(\det[\mathbf{M}(\mathbf{r}')]) \right]}. \tag{39}$$

The above expression suggests that this imaginary-time sampling technique can be performed with an effective PES of (P+1)-bead open chain,

$$\tilde{V}(\mathbf{r}) = W(\mathbf{r}) + V_{\text{spr}}(\mathbf{r}) + \overline{V}_{\text{OP}}(\mathbf{r}), \tag{40}$$

where the first term is from Gaussian integral and couples all the beads. This term is also complex for the general two-state case [due to term $-\frac{it}{4P\hbar}\Delta V''(r^{(\alpha)})$ of **M** matrix in Eq. (34) and term $-\frac{i\beta}{4P}\Delta V'(r^{(\alpha)})$ of vector **K** in Eq. (35)],

$$W(\mathbf{r}) = \frac{1}{2\beta} \left[\mathbf{K}(\mathbf{r})^T \mathbf{M}^{-1}(\mathbf{r}') \mathbf{K}(\mathbf{r}) + \ln(\det[\mathbf{M}(\mathbf{r}')]) \right]_{\text{complex}}, \quad (41)$$

the second term contains harmonic interactions between adjacent beads with frequency $\omega_P = \sqrt{P}/|\tau_c|$,

$$V_{\rm spr}(\mathbf{r}) = \sum_{\alpha=1}^{P} \frac{1}{2} m \omega_P^2 (r^{(\alpha+1)} - r^{(\alpha)})^2, \tag{42}$$

and the last term reflects the open-chain potential energy on the average PES with the two end beads subject to only half the average PES.

$$\overline{V}_{\mathrm{OP}}(\mathbf{r}) = \frac{1}{p} \left[\sum_{\alpha=2}^{p} \overline{V}(r^{(\alpha)}) + \frac{1}{2} \overline{V}(r^{(1)}) + \frac{1}{2} \overline{V}(r^{(P+1)}) \right]. \tag{43}$$

In fact, this imaginary-time path integral can be evaluated using any sampling technique, e.g., Monte Carlo, molecular dynamics (MD), or any enhanced sampling scheme. When using MD to sample openchain configurations, fictitious masses (m') and fictitious momenta $\mathbf{p} = (p^{(1)}, \dots, p^{(P+1)})$ are added to form a Hamiltonian,

$$\tilde{H}(\mathbf{r},\mathbf{p}) = \frac{\mathbf{p}^2}{2m'} + \tilde{V}(\mathbf{r}). \tag{44}$$

It is important to note that when $\Delta V \equiv 0$, $G_{AD}(t)$ reduces to the single-state case for the average PES, where the phase factor $e^{i\Phi}$ originating from the electronic quantum coherence vanishes and the $W(\mathbf{r})$ reduces to the single-state counterpart on the average PES, i.e., $W_{\rm av}(\mathbf{r})$, which is real. Let us denote the OCPI sampling distribution of the open chain on the average PES as

$$\tilde{\rho}_{\text{av}} = \frac{(2\pi)^{(P-1)/2}}{\tilde{Z}_{\text{av}}} \exp(-\beta \tilde{V}_{\text{av}}(\mathbf{r})), \tag{45}$$

$$\tilde{Z}_{\text{av}} = (2\pi)^{(P-1)/2} \int d\mathbf{r} \, \exp(-\beta \tilde{V}_{\text{av}}(\mathbf{r})), \tag{46}$$

where the OCPI effective potential, dependent on the average PES, is given by

$$\tilde{V}_{av}(\mathbf{r}) = W_{av}(\mathbf{r}) + V_{spr}(\mathbf{r}) + \overline{V}_{OP}(\mathbf{r}), \tag{47}$$

$$W_{\text{av}}(\mathbf{r}) = \frac{1}{2\beta} \left[\mathbf{K}(\mathbf{r})^T \mathbf{M}^{-1}(\mathbf{r}') \mathbf{K}(\mathbf{r}) + \ln(\det[\mathbf{M}(\mathbf{r}')]) \right]_{\text{av}}.$$
 (48)

Here, $W_{av}(\mathbf{r})$ is positive definite. The single-state symmetrized TCF [Eq. (2)] on the average PES is expressed as

$$G(t) = \int d\mathbf{r} \tilde{\rho}_{av}(\mathbf{r}) A(r^{(1)}) B(r^{(P+1)})$$
$$= \left\langle A(r^{(1)}) B(r^{(P+1)}) \right\rangle_{av}. \tag{49}$$

However, in the two-state case, $W(\mathbf{r})$ is complex and not positive definite; thus, it cannot be used as sampling distribution.

To evaluate the two-state $G_{AD}(t)$ in Eq. (39), we utilize importance sampling and propose to sample according to \tilde{V}_{av} with the real $W_{av}(\mathbf{r})$ and absorb the ratio $e^{-\beta W(\mathbf{r})}/e^{-\beta W_{av}(\mathbf{r})}$ in the observable,

$$G_{AD}(t) = \frac{\tilde{Z}_{av}}{Z_D} \frac{(2\pi)^{(P-1)/2}}{\tilde{Z}_{av}} \int d\mathbf{r} \rho_1(\mathbf{r}) \Gamma_{DA}(\mathbf{r}^{(1)}) \Gamma_{AD}(\mathbf{r}^{(P+1)})$$

$$\times e^{i\Phi(\mathbf{r})} \frac{e^{-\beta W(\mathbf{r})}}{e^{-\beta W_{av}(\mathbf{r})}} e^{-\beta W_{av}(\mathbf{r})}$$

$$= \frac{\tilde{Z}_{av}}{Z_D} \left\{ \Gamma_{DA}(\mathbf{r}^{(1)}) \Gamma_{AD}(\mathbf{r}^{(P+1)}) e^{i\Phi(\mathbf{r})} \frac{e^{-\beta W(\mathbf{r})}}{e^{-\beta W_{av}(\mathbf{r})}} \right\}_{av}. \tag{50}$$

The above formula provides a practical approach for evaluating the two-state $G_{AD}(t)$, and we shall employ it in our calculations of open path integral molecular dynamics (OPIMD). ^{31,58,59} We note that there are surely other ways to evaluate $G_{AD}(t)$, such as open path-integral Monte Carlo, ⁴⁰ complex Langevin methods, ⁶⁰ and other enhanced sampling techniques. Moreover, the two-state OCPI could be systematically improved by, for example, considering a higher-order expansion in the difference variables via cumulant methods, ⁴¹ tuning the optimal value of P as in colored-noise thermostat approaches, and employing higher-order Trotter expansions such as a Suzuki–Chin factorization. ^{41,61}

III. MODEL

The spin-boson model is one of the most widely used twostate models for quantum dynamics simulations of charge transfer reactions; the Hamiltonian is given by 50,51

$$\hat{H} = \Gamma \hat{\sigma}_x - \frac{\Delta E}{2} \hat{\sigma}_z + \sum_{j=1}^{N} \left(\frac{\hat{P}_j}{2} + \frac{1}{2} \omega_j^2 \hat{R}_j^2 - c_j \hat{R}_j \hat{\sigma}_z \right), \tag{51}$$

where $\hat{\sigma}_x = |D\rangle\langle A| + |A\rangle\langle D|$ and $\hat{\sigma}_z = |D\rangle\langle D| - |A\rangle\langle A|$ are Pauli spin operators; $\Delta E = -\hbar\omega_{DA}$ is the reaction free energy for $D \to A$ process; $\{\hat{R}_j, \hat{P}_j, \omega_j, c_j | j = 1, \dots, N\}$ are the mass-weighted positions, momenta, nuclear vibrational frequencies, and the electronic–nuclear coupling coefficients, respectively; and N is the number of nuclear DOFs.

Equivalently, the spin-boson Hamiltonian in Eq. (51) can be cast into the general form of Eq. (5), where the electronic couplings $\hat{\Gamma}_{DA} = \hat{\Gamma}_{AD} = \Gamma$ and the donor-state and acceptor-state nuclear Hamiltonians are given by 46

$$\hat{H}_{D} = \sum_{j=1}^{N} \frac{\hat{P}_{j}^{2}}{2} + \frac{1}{2}\omega_{j}^{2}\hat{R}_{j}^{2} + \hbar\omega_{DA},$$

$$\hat{H}_{A} = \sum_{j=1}^{N} \frac{\hat{P}_{j}^{2}}{2} + \frac{1}{2}\omega_{j}^{2}(\hat{R}_{j} - R_{j}^{eq})^{2}.$$
(52)

Here, R_j^{eq} is the equilibrium position displacement between the donor and acceptor states for the *j*th nuclear mode, which is related to c_i through

$$R_j^{\text{eq}} = \frac{2c_j}{\omega_i^2}$$
 (j = 1,...,N). (53)

The reorganization energy for the spin-boson model is

$$E_r = \sum_{j=1}^{N} \frac{2c_j^2}{\omega_j^2} = \frac{1}{2} \sum_{j=1}^{N} \omega_j^2 \left(R_j^{\text{eq}}\right)^2.$$
 (54)

The frequencies and the coupling coefficients $\{\omega_j, c_j\}$ in the spin-boson model are usually determined by the spectral density defined by 50

$$J(\omega) = \frac{\pi}{2} \sum_{j=1}^{N} \frac{c_j^2}{\omega_j} \delta(\omega - \omega_j), \tag{55}$$

which can be constructed using the energy-gap time correlation function obtained from all-atom molecular dynamics simulations of realistic condensed-phase systems. ^{52,62,63} In this work, we employ the Ohmic spectral density given by

$$J(\omega) = \frac{\pi}{2} \hbar \xi \omega e^{-\omega/\omega_c},\tag{56}$$

where ω_c is a cutoff frequency and ξ is the Kondo parameter. The nuclear mode frequencies and couplings for the Ohmic spectral density can be obtained using⁶⁴

$$\omega_j = -\omega_c \ln \left(1 - \frac{j}{N+1} \right) \quad (j=1, \ldots, N), \tag{57}$$

$$c_j = \omega_j \sqrt{\hbar \xi \omega_c / (N+1)} \quad (j=1, \ldots, N).$$
 (58)

In this study, we choose the model parameters $\omega_c = 1$, $\hbar = 1$, $\xi = 1$, $\Gamma = 1$, and N = 19. In the rest of the paper, the energy unit is chosen as $\hbar \omega_c$ and the time unit as ω_c^{-1} . We investigate two temperatures, $\beta = 0.5$ and 4, as high and low temperatures, respectively.

For the spin-boson model, the symmetrized TCF $G_{AD}(t)$ is known in closed form as

$$G_{AD}(t) = \Gamma^{2} \exp \left\{ -i\omega_{DA}t - \sum_{j=1}^{N} \frac{\omega_{j}(R_{j}^{\text{eq}})^{2}}{2\hbar} \times \left[\coth\left(\frac{\beta\hbar\omega_{j}}{2}\right) \left(1 - \cos(\omega_{j}t)\cosh\left(\frac{\beta\hbar\omega_{j}}{2}\right)\right) + \cos(\omega_{j}t)\sinh\left(\frac{\beta\hbar\omega_{j}}{2}\right) \right] \right\},$$
 (59)

which is a real even function of time when $\omega_{DA} = 0$. The quantum TCF $C_{AD}(t)$ is also known in closed form,⁴⁶

$$C_{AD}(t) = C_{DA}^{*}(t) = \Gamma^{2} \exp \left\{ -i\omega_{DA}t - \sum_{j=1}^{N} \frac{\omega_{j}(R_{j}^{\text{eq}})^{2}}{2\hbar} \right.$$
$$\times \left[\coth \left(\frac{\beta\hbar\omega_{j}}{2} \right) (1 - \cos(\omega_{j}t)) - i \sin(\omega_{j}t) \right] \right\}. \tag{60}$$

Time integration of Eq. (60) leads to the FGR rate constant, which is equivalent to the Fourier transform of the $C_{AD}(t; \omega_{DA} = 0)$ or the inverse Fourier transform of the $C_{DA}(t; \omega_{DA} = 0)$ as a function of ω_{DA} ,

$$k(\omega_{DA}) = \frac{1}{\hbar^2} \mathcal{F}[C_{AD}(t; \omega_{DA} = 0)](\omega_{DA})$$
$$= \frac{1}{\hbar^2} \mathcal{F}^{-1}[C_{DA}(t; \omega_{DA} = 0)](\omega_{DA}). \tag{61}$$

This procedure for obtaining the FGR rate constant from $G_{AD}(t)$ from imaginary-time OCPI sampling is summarized in Fig. 2.

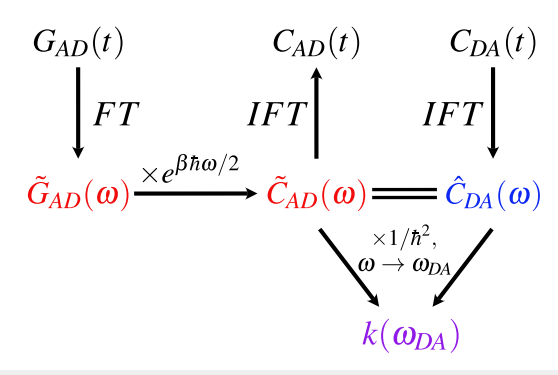


FIG. 2. Procedure of calculating FGR rate constant $k(\omega_{DA})$ from the symmetrized TCF $G_{AD}(t)$ without $\Delta E = -\hbar \omega_{DA}$. Here, FT stands for Fourier transform, $\tilde{A}(\omega) = \mathcal{F}[A(t)](\omega)$, and IFT stands for inverse Fourier transform, $\hat{A}(\omega) = \mathcal{F}^{-1}[A(t)](\omega)$. Finally, the FGR rate constant as a function of ω_{DA} is given by $k(\omega_{DA}) = \tilde{C}_{AD}(\omega_{DA}) / \hbar^2 = \hat{C}_{DA}(\omega_{DA}) / \hbar^2$.

IV. COMPUTATIONAL DETAILS

In the OCPI calculations, we employed imaginary-time open path integral molecular dynamics (OPIMD) with staging variables 33,59 for sampling open chains of the spin-boson model at the two temperatures $\beta=0.5$ and $\beta=4$. A Langevin thermostat 65 was implemented for a canonical sampling of the open-chain configuration space. The $G_{AD}(t)$ was evaluated starting from t=0 with a physical time interval $\Delta t=0.11$ and a maximum physical time 14.08, at a total of 129 time points; negative physical times were directly obtained by using time-symmetry of $G_{AD}(t)$. The number of beads P ranged from 64 to 284, and more specifically, we added beads according to

$$P = \max[64, \text{ integer}(20|\tau_c|)], \tag{62}$$

to increase numerical stability in long physical time regions. This scheme of choosing P leads to a constant P=64 when t<3.3 at $\beta=0.5$ and t<2.53 at $\beta=4$ before P starts to increase with the physical time.

In the imaginary-time OCPI simulations, the MD time step δt of the simulations ranged from 0.002 to 0.010. In all cases, the open chains were first propagated for 1×10^6 steps for equilibration, and then configurations of the open chains for each nuclear mode were sampled in subsequent MD steps. In the high-temperature case ($\beta = 0.5$), the MD time step was chosen to be $\delta t = 0.010$ and $\delta t = 0.002$ for modes 0–9 and modes 10–18, respectively, and a total of 4×10^9 and 5×10^8 were sampled for modes 0-2 and modes 3–18, respectively. In the low-temperature case ($\beta = 4$), the MD time step was chosen to be $\delta t = 0.010$ for all modes, and a total of 4×10^9 , 2×10^9 , and 5×10^8 were sampled for modes 0-2, modes 3-9, and modes 10-18, respectively. Statistical properties, such as the average effective energy and average interbead and end-to-end distances, were obtained by sampling every 10³ configurations in the OCPI simulations. The computational cost for sampling 10⁹ open-chain configurations of all time points per mode is about 9900 core-hours using a single core of Intel Xeon Gold 6132 @ 2.60 GHz CPU. The computational cost grows linearly with the number of nuclear normal modes in the spin-boson model, whereas for coupled nuclear degrees of freedom, it is expected to grow beyond linear scaling, and the sparsity of the $\bf M$ matrix would depend on the coupling between the modes. Furthermore, from our observation, the computational cost grows approximately quadratically with respect to the number of beads. For example, sampling of 10^9 open-chain configurations of 66 beads takes 55 000 s on one core and sampling of 10^9 open-chain configurations of 134 beads takes 190 000 s.

A Whittaker–Eliers (WE) smoother,⁶⁶ implemented in Python,⁶⁷ is employed iteratively to smooth the numerically sampled $G_{AD}(t)$. Three parameters for the WE smoother include the order of the fitting polynomial (n), the smoothness parameter (λ) , and a convergence tolerance (D_{conv}) . The input data to the smoother is $\log G_{AD}(t)$, where \log denotes a base-10 logarithm hereinafter. In the low-temperature case, we used an iterative WE smoother with n=4, $\lambda=1\times10^3$, and $D_{\text{conv}}=1\times10^{-4}$; in the high-temperature case, the central 110 data points were smoothed with n=4, $\lambda=10$, and $\mathcal{D}_{\text{conv}}=5\times10^{-4}$.

There is a normalization factor $\tilde{Z}_{\rm av}/Z_D$ in Eq. (50) corresponding to the different partition functions in the definition of two-state symmetrized TCF $G_{AD}(t)$ in Eq. (13) and the OCPI partition function for the average PES as in Eq. (46). Since the OCPI partition function \tilde{Z}_D is equal to the quantum partition function Z_D for harmonic potentials as in the spin-boson model, for a nuclear mode, we can transform this normalization factor by substituting $r^{(\alpha)} \rightarrow r^{(\alpha)} + \frac{1}{2}R^{\rm eq}$, $(\alpha = 1, \ldots, P+1)$ in the OCPI effective potential for the average PES [Eq. (47)] and compare with the OCPI effective potential for the donor-state PES,

$$\tilde{V}_{D}(\mathbf{r}) = \frac{1}{2\beta} \left[\mathbf{K}(\mathbf{r})^{T} \mathbf{M}^{-1}(\mathbf{r}') \mathbf{K}(\mathbf{r}) + \ln(\det[\mathbf{M}(\mathbf{r}')]) \right]_{D}$$

$$+ \sum_{\alpha=1}^{P} \frac{1}{2} m \omega_{P}^{2} (r^{(\alpha+1)} - r^{(\alpha)})^{2}$$

$$+ \frac{1}{P} \left[\sum_{\alpha=2}^{P} V_{D}(r^{(\alpha)}) + \frac{1}{2} V_{D}(r^{(1)}) + \frac{1}{2} V_{D}(r^{(P+1)}) \right]. \quad (63)$$

Consider the *j*th mode with open-chain variables $\mathbf{r}_j = (r_j^{(1)}, \ldots, r_j^{(P+1)})$. On introducing a change of variables $r_j^{(\alpha)} \to r_j^{(\alpha)} + \frac{1}{2} R_j^{\mathrm{eq}}$ $(\alpha = 1, \ldots, P+1)$ and inserting $V_D(\hat{R}_j) = \frac{1}{2} \omega_j^2 \hat{R}_j^2$ and $\overline{V}(\hat{R}_j) = \frac{1}{2} \omega_j^2 (\hat{R}_j) - \frac{1}{2} R_j^{\mathrm{eq}} + \frac{1}{8} \omega_j^2 (R_j^{\mathrm{eq}})^2$ into Eqs. (47) and (63), respectively, we obtain

$$\bar{V}_{\text{av}}\left(\mathbf{r}_j + \frac{1}{2}R_j^{\text{eq}}\right) = \bar{V}_D(\mathbf{r}_j) + \frac{1}{8}\omega_j^2 (R_j^{\text{eq}})^2.$$
 (64)

Hence, for the jth mode,

$$\tilde{Z}_{\text{av}} = (2\pi)^{(P-1)/2} \int d\mathbf{r}_{j} e^{-\beta \tilde{V}_{\text{av}}(\mathbf{r}_{j})}
= (2\pi)^{(P-1)/2} \int d\mathbf{r}_{j} e^{-\beta \left[\tilde{V}_{D}(\mathbf{r}_{j}) + \frac{1}{8}\omega_{j}^{2}(R_{j}^{\text{eq}})^{2}\right]}
= \tilde{Z}_{D}e^{-\beta \frac{1}{8}\omega_{j}^{2}(R_{j}^{\text{eq}})^{2}},$$
(65)

and the normalization factor for all the modes of the spin-boson model is given by

$$\frac{\tilde{Z}_{\rm av}}{\tilde{Z}_{\rm D}} = e^{-\beta \frac{1}{8} \sum_{j=1}^{N} \omega_j^2 (R_j^{\rm eq})^2} = e^{-\beta E_r/4}.$$
 (66)

The real-time LSC/LPI method for calculating the FGR CT rate constant was implemented as a trajectory-based numerical simulation⁴⁶ and used to compare with the imaginary-time OCPI approach. The quantum TCF obtained directly from LSC/LPI simulation for the spin-boson model is given by

$$C_{DA}^{LSC/LPI}(t) = \Gamma^{2} \int d\mathbf{R}_{0} d\mathbf{P}_{0} \, \rho_{D,W}^{eq}(\mathbf{R}_{0}, \mathbf{P}_{0})$$

$$\times \exp\left[-\frac{i}{\hbar} \int_{0}^{t} \Delta V(\mathbf{R}_{\tau}^{av}) d\tau\right], \tag{67}$$

where the initial conditions $(\mathbf{R}_0, \mathbf{P}_0)$ were sampled from the Wigner semiclassical distribution corresponding to the equilibrated donor state,

$$\rho_{D,W}^{\text{eq}}(\mathbf{R}_0, \mathbf{P}_0) = \prod_{j=1}^{N} \frac{1}{\pi \hbar} \tanh\left(\frac{\beta \hbar \omega_j}{2}\right) \times \exp\left\{-\frac{2}{\hbar \omega_j} \tanh\left(\frac{\beta \hbar \omega_j}{2}\right) \left(\frac{P_{j0}^2}{2} + \frac{\omega_j^2 R_{j0}^2}{2}\right)\right\}, \quad (68)$$

and then the nuclear positions and momenta were propagated on the average PES with MD time step $\delta t = 0.001$ and along each trajectory from physical time t = 0 to $t = \pm 14.08$. The quantum TCF as a function of time with interval $\Delta t = 0.11$ was obtained by averaging over 10^6 trajectories and total 2.56×10^8 configurations. The computational cost for generating 10^6 trajectories is about 15 core-hours using a single core of Intel Xeon Gold 6132 @ 2.60 GHz CPU.

V. RESULTS AND DISCUSSION

Our main result is shown in Fig. 3, where the CT rate constants in the spin-boson model computed using the proposed imaginarytime two-state open-chain path-integral technique, the real-time LSC/LPI approach, and the analytical FGR rate constants are compared for two temperatures ($\beta = 0.5$ and $\beta = 4$). First, we see that the OCPI approach is able to reproduce the analytical FGR CT rate constant in the typical turnover parameter space ranging from the normal regime to the inverted regime while increasing the thermodynamic driving force or the reaction free energy $-\Delta E = \hbar \omega_{DA}$. This is an important test of the ability of the two-state OCPI approach to capture the real-time quantum dynamical behavior using only imaginary-time sampling, which makes OCPI promising for systems that are not straightforward to formulate as a real-time quantum dynamical scheme. In addition, using the WE smoother, 66 the twostate OCPI approach can reproduce the analytical FGR CT rate constant in a much wider region. The effect of smoothing actually helps in reducing numerical noise in the short-time signal of $G_{AD}(t)$, which has a significant effect on the FGR rate constant in the large ω_{DA} region. This was confirmed by the identical FGR rate constants obtained using smoothed short-time (up to t = 5.5) and long-time (up to t = 14) inputs. Second, both the imaginary-time OCPI and the real-time LSC/LPI methods generate accurate FGR

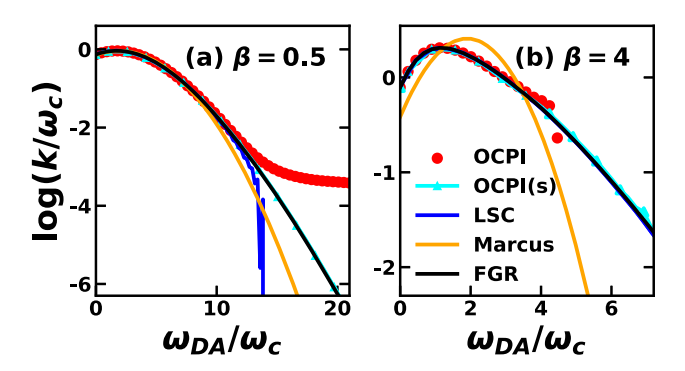


FIG. 3. Comparison of the charge transfer rate constants obtained with imaginary-time open-chain path-integral (OCPI, red circle), smoothed OCPI numerical result (OCPI(s), cyan dashed line), real-time linearized semiclassical (LSC, blue), Marcus theory (orange) against analytical Fermi's golden rule (FGR, black) for the spin-boson model at temperatures (a) $\beta=0.5$ and (b) $\beta=4$. The logarithm with base 10 of the rate constant is plotted as a function of ω_{DA}/ω_c corresponding to a variety of thermodynamic driving force ($-\Delta E=\hbar\omega_{DA}$).

CT rate constant until they start to deviate from the exact result since $\omega_{DA}=11~\omega_c$ at high temperature $\beta=0.5$ [Fig. 3(a)], whereas at low temperature, the OCPI method starts to deviate from the exact result at $\omega_{DA}=4.5~\omega_c$, which is earlier than the LSC/LPI method [Fig. 3(b)]. Since the OCPI and LSC/LPI are numerically "exact" for the spin-boson model with harmonic nuclear modes, the observed deviations are ascribed to numerical issues such as the sign problem in the real-time path-integral approach as well as the sampling of the open chains and the exponential conversion factor in the imaginary-time OCPI approach, which will be discussed later. Third, the Marcus theory seems to be able to predict the high-temperature CT rate constant rather well when $\omega_{DA}<10~\omega_c$ at $\beta=0.5$ but breaks down for the entire range of ω_{DA} in the low-temperature $\beta=4$ case dramatically, which indicates the importance of incorporating the nuclear quantum effects in calculating CT rate constant, as addressed in FGR.

The direct results from the imaginary-time OCPI simulations of the spin-boson model at two temperatures are the two-state $G_{AD}(t)$ shown in Fig. 4. For the spin-boson model with $\omega_{DA}=0$, the two-state symmetrized TCF $G_{AD}(t)$ is a real and even function of time, so we extended the positive time result to negative using symmetry. The numerical results of $G_{AD}(t)$ at two temperatures are reproduced with extremely high accuracy, for 20 orders of magnitude for the β = 0.5 case and 7 orders of magnitude for the β = 4 case. The smoothed $G_{AD}(t)$ perfectly reproduces the exact result. Figures 4(e) and 4(f) suggest that the OCPI sampling error is quite small, where the largest error of $G_{AD}(t)$ is 10^{-3} for the high-temperature case and 10⁻⁴ for the low-temperature case. These results suggest that the OCPI sampling scheme using Eq. (50) offers the two-state symmetrized TCF with amazingly high accuracy even with the complex observable, at least for the current benchmark spin-boson model.

We, thus, know that the two-state symmetrized TCF is accurately reproduced using OCPI. To further analyze the origin of the CT rate constant deviation at large ω_{DA} by the current OCPI method, we plot the relevant intermediate TCFs and their frequency-domain

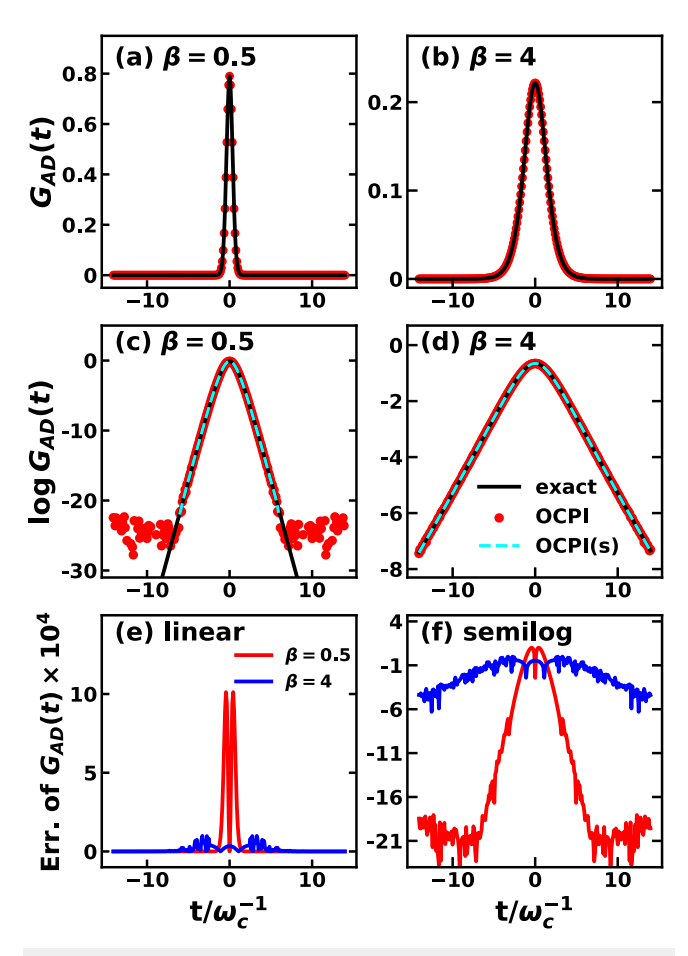


FIG. 4. Two-state symmetrized time correlation functions $G_{AD}(t)$ of the spin-boson model obtained with numerical imaginary-time OCPI sampling (red circle), smoothed OCPI numerical results (cyan dashed line), and analytical result (black line) plotted in the linear scale for temperatures (a) $\beta=0.5$ and (b) $\beta=4$; the corresponding semilog scale plots are included in panels (c) and (d). (e) and (f) Absolute errors of the numerical $G_{AD}(t)$ for both temperatures at $\beta=0.5$ (red) and $\beta=4$ (blue) plotted in the linear and semilog scales, respectively.

counterparts in the conversion steps from the two-state symmetrized TCF $G_{AD}(t)$ to the corresponding standard TCF $C_{AD}(t)$ at $\beta=0.5$ in Fig. 5. Taking Fourier transform on the time-domain two-state symmetrized TCF $G_{AD}(t)$ that is directly obtained from OPSCF calculation [Fig. 5(a)], we obtain the frequency-domain $\tilde{G}_{AD}(\omega)$ [Fig. 5(b)], where we see a symmetric deviation of the numerical result from the analytical result. Then, using the relation $\tilde{C}_{AD}(\omega) = e^{\beta\hbar\omega/2}\tilde{G}_{AD}(\omega)$ in Eq. (14), we obtain the frequency-domain $C_{AD}(\omega)$ [Fig. 5(c)], where we see that the numerical result shows a larger error in the positive frequency region than the negative region. The FGR rate constant as a function of ω_{DA} is proportional to $C_{AD}(\omega)$, thus the intrinsic conversion factor of $e^{\beta\hbar\omega/2}$ magnifies the deviation in the FGR rate constant. The magnification of deviation is more pronounced in the low-temperature case of $\beta=4$. It is evident that the exponential factor between $\tilde{G}_{AD}(\omega)$ and $\tilde{C}_{AD}(\omega)$

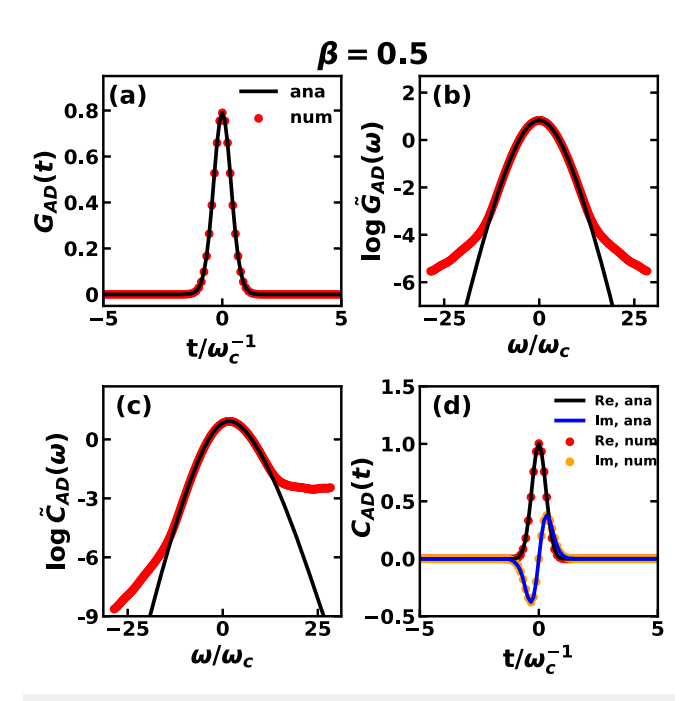


FIG. 5. The conversion from the two-state symmetrized time correlation function to the standard quantum time correlation function at $\beta=0.5$ as described by Fig. 2, where the numerical and analytical results are rendered as scatter dots and lines, respectively. (a) The two-state symmetrized TCF, $G_{AD}(t)$, in linear scale; (b) Fourier transformed symmetrized TCF, $\tilde{G}_{AD}(\omega)$, in semilog scale; (c) Fourier transformed quantum TCF, $\tilde{C}_{AD}(\omega)$, in semilog scale; (d) the quantum TCF, $C_{AD}(t)$, in the linear scale with the numerical real and imaginary parts as red and orange circles compared with analytical real and imaginary parts as black and blue lines, respectively.

magnifies the sampling error in the OCPI and leads to the error of the predicted FGR rate constant at large ω_{DA} or the deep inverted regime. Finally, the standard two-state TCF $C_{AD}(t)$ is obtained from an inverse Fourier transform of $\tilde{C}_{AD}(\omega)$ back to the time-domain as shown in [Fig. 5(d)], which reproduces the analytical TCF.

Next, we discuss the features of the open chains in the OCPI simulations of the spin-boson model. Figure 6 shows the decomposition of the average OCPI effective potential energy for three representative nuclear modes (modes 5, 10, 15) as a function of physical time at two temperatures (β = 0.5 on left panels and β = 4 on right panels). According to Eq. (50), the OCPI effective potential is given by Eq. (47) or expressed as follows:

$$\tilde{V} = V_{\text{spr}} + \overline{V}_{\text{OP}} + \frac{1}{2\beta} \left[\mathbf{K}^T \mathbf{M}^{-1} \mathbf{K} + \ln(\det \mathbf{M}) \right]_{\text{av}}.$$
 (69)

From top to bottom rows in Fig. 6, we have $V_{\rm spr}$, $\overline{V}_{\rm OP}$, $\frac{1}{2\beta}{\bf K}^T{\bf M}^{-1}{\bf K}$, and $\frac{1}{2\beta}\ln(\det{\bf M})$ terms, and the last row is the total effective potential. It is clearly shown that the $\frac{1}{2\beta}\ln(\det{\bf M})$ term is dominant among all the contributions, which is typically 2 orders of magnitude larger than the other terms. The origin of the curvature of the $\frac{1}{2\beta}\ln(\det{\bf M})$ term changes at around t=2.5, especially

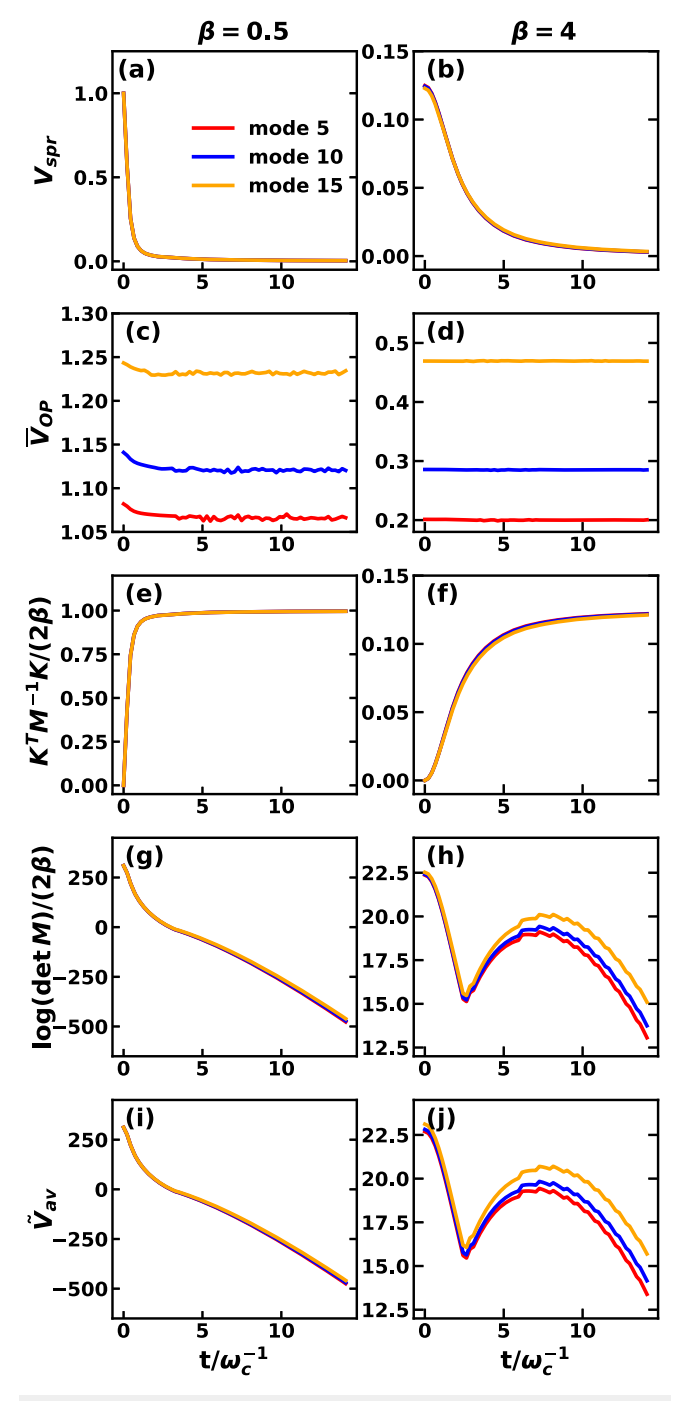


FIG. 6. ecomposition of the averaged OCPI effective potential energy for representative low, medium, and high frequency modes of the spin-boson model as a function of time (mode 5, mode 10, and mode 15 as red, blue, and orange lines) at temperatures $\beta=0.5$ (left panels) and $\beta=4$ (right panels). Panels (a) and (b), (c) and (d), (e) and (f), (g) and (h), and (j) and (j) correspond to the interbead spring potential energy V_{spr} , open path potential energy on average PES \overline{V}_{OP} , the $\frac{1}{2\beta}\mathbf{K}^T\mathbf{M}^{-1}\mathbf{K}$ term, the $\frac{1}{2\beta}\ln(\det \mathbf{M})$ term, and the total OCPI effective potential energy \tilde{V} , respectively.

in Fig. 6(h), and can be traced back to the fact that our choice of the bead number P starts to increase linearly with complex time $|\tau_c|$ at longer times according to Eq. (62). The large magnitude change in the $\frac{1}{2\beta}\ln(\det\mathbf{M})$ term lies in the fact that when P is fixed, this term scales as $P\ln(A)\approx P\ln(P\beta/|\tau_c|^2)+\mathrm{Const.}$ $\approx -2\ln(|\tau_c|)+\mathrm{Const.}$, when $P\propto |\tau_c|$, it reduces to $-|\tau_c|\ln(|\tau_c|)+\mathrm{Const.}$, and at low temperature, increasing the bead number affects this trend more distinctly. Moreover, V_{spr} decreases with increasing time since the interbead frequency $\omega_P = \sqrt{P}/|\tau_c|$ increases with the number of beads, whereas $\frac{1}{2\beta}\mathbf{K}^T\mathbf{M}^{-1}\mathbf{K}$ shows the opposite trend such that it roughly cancels with V_{spr} . The $\overline{V}_{\mathrm{OP}}$ term has a relatively stable behavior for different times, which indicates that the open-chain beads remain near the minimum of the average PES.

The typical structural descriptors for the open chains include the average interbead distance between connected beads and the average end-to-end distance between the first and the last open-chain beads, which are defined as follows:

$$D_{\text{interbead}}(t) = \left\langle \frac{1}{P} \sum_{\alpha=1}^{P} \left| r^{(\alpha+1)} - r^{(\alpha)} \right| \right\rangle_{\text{av}}, \tag{70}$$

$$D_{\text{end-end}}(t) = \left\{ \left| r^{(1)} - r^{(P+1)} \right| \right\}_{\text{av}}.$$
 (71)

Figure 7 displays the average interbead and end-to-end distances of open chains for the three representative modes (modes 5, 10, 15) at $\beta=0.5$ and $\beta=4$, respectively. The averaged interbead distances for high and low temperatures, as shown in Figs. 7(a) and 7(b), respectively, initially rise when t<2.5 and then decay when t>2.5. This trend comes from the bead number choice, i.e., before t=2.5, the bead number P is fixed at 64 and, thus, the interbead frequency $\omega_P=\sqrt{P}/|\tau_c|$ decreases with increasing time, which will make the open chain more delocalized, whereas after t=2.5, the bead number P starts to increase, resulting in more compact and localized open chains.

The averaged end-to-end distances for high and low temperatures are shown in Figs. 7(c) and 7(d), respectively. The end-to-end distances for three modes of different frequencies clearly reflect their physical periodic motion, where the first peaks of the oscillation in the end-to-end distances match exactly with the half periods of the three modes [as indicated by arrows in Figs. 7(c) and 7(d)]. The end-to-end distance clearly exhibits the real-time dynamics, which demonstrates that the OCPI approach accurately captures the real-time quantum dynamics via a well-defined sampling scheme; thus, to be more precise, we should refer to the OCPI a "complextime" path-integral technique. Unlike the ring-polymer beads that are equivalent in imaginary-time RPMD and CMD approaches, the open-chain beads are associated with increasing time slices: The first bead of the open chain corresponds to time zero while the last bead of the open chain corresponds to the time t, and the intermediate beads follow a chronological order in-between time zero and t. Efficient sampling of the open-chain configurations in the effective potential is thus key to the OPCI method.

Figure 8 presents several sampled open-chain snapshots for the three representative modes (modes 5, 10, 15) at the two temperatures. It is evident that the open chains at high temperature ($\beta = 0.5$)

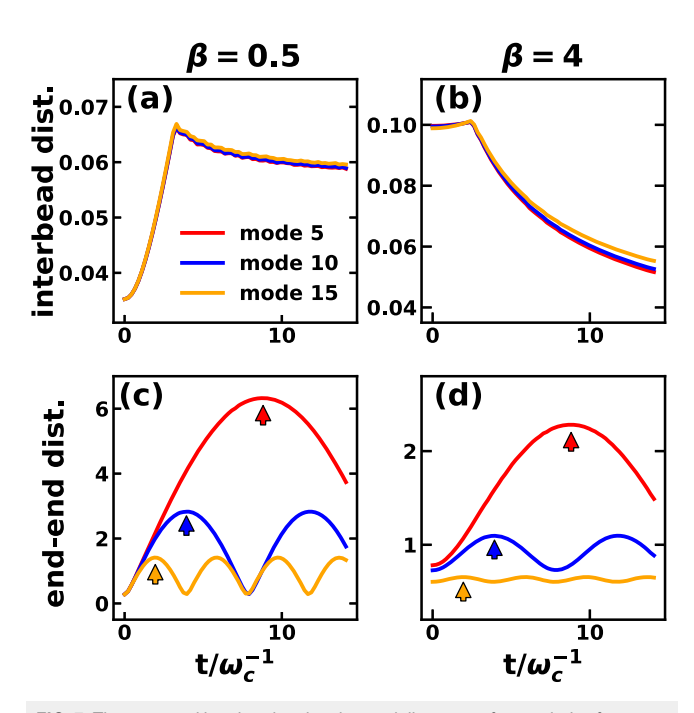


FIG. 7. The averaged interbead and end-to-end distances of open chains for representative low, medium, and high frequency modes of the spin-boson model (mode 5, mode 10, and mode 15 as red, blue, and orange lines). Panels (a) and (b) are the averaged interbead distances between connected beads [Eq. (70)] for $\beta=0.5$ and $\beta=4$, respectively. Panels (c) and (d) are the averaged end-to-end distances between the first and the last open-chain beads [Eq. (71)] for $\beta=0.5$ and $\beta=4$, respectively, and the arrows indicate the half period of the corresponding modes.

are smoother than those at low temperature ($\beta = 4$) in all the cases sampled, which can be traced back to the fact that the interbead frequency ω_P is larger at high temperature than at low temperature. Thus, the open-chain beads are more spread or delocalized at low temperature than at high temperature. A more important observation is that with an increase of the real time from t = 0 to t = 10, the bead positions from the first bead to the last one exhibit a physical oscillation with the corresponding mode's frequency. For example, for mode 5 at high temperature, the bead positions barely change at t = 0, whereas at t = 10, about three-quarters of an oscillation is seen; for mode 10 at high temperature, a similar trend is observed except for a higher oscillation frequency. This is more obvious in the case of mode 15 in the high-temperature case, there is nearly one period at t = 2.5, two periods at t = 5, and so on. In the low-temperature case, the bead positions also exhibit the same physical oscillation of the corresponding frequency but with more noise than in the high-temperature case. Moreover, the sampled open chains start from different initial bead positions that span the typical region of the corresponding mode at a given temperature, which can be seen from the wider distribution of bead positions at high temperature than at low temperature. In short, snapshots of the open-chain sampling display a delocalization effect at low temperature and periodic motion of the bead positions with a frequency that increases with time.

Finally, we discuss the features and possible improvements regarding the two-state OCPI technique. First, the current computational approach has a complex phase factor $e^{i\Phi(\mathbf{r})}e^{-\beta W(\mathbf{r})}/e^{-\beta W_{av}(\mathbf{r})}$ in the observable in Eq. (50), allowing us to sample only from positive-definite OCPI effective potential \tilde{p}_{av} . Although this importance sampling approach works for the model tested, there may exist an alternative and more effective approach where one could directly sample from complex effective potential. When performing the imaginary-time sampling over a complex effective Hamiltonian, the observable will contain only one complex factor $e^{i\Phi(\mathbf{r})}$ resulting from the energy-gap fluctuation that embodies the electronic quantum coherence, a signature of two-state TCF.

Second, the normalization factor \tilde{Z}_{av}/Z_D , in general, does not have a closed-form expression for arbitrary molecular systems and may require a separate calculation to determine the ratio of partition functions using enhanced sampling λ -dynamics⁴⁵ or more complicated sampling techniques to compute the partition functions themselves.⁶⁸

Third, compared with the real-time LSC/LPI approach, the efficiency of this imaginary-time OCPI approach currently does not exceed the real-time LSC/LPI, since the OCPI requires independent simulations for each different physical time, whereas the trajectory-based LSC/LPI could obtain all the times from averaging over the large set of trajectories. The fact that OCPI is implemented as a set of independent sampling calculations makes it more suitable for parallel computing. The Wigner distribution for LSC/LPI method is not easy to obtain for anharmonic systems, 18,19,69,70 but in OCPI, the effective distribution will be accurate up to the second order in the difference path variables, which is more straightforward to implement than obtaining the Wigner distribution for general anharmonic systems. In anharmonic systems, the Wigner transformed density may be nonpositive-definite and suffer from multidimensional Fourier transform issues. Moreover, there is room for improving OCPI calculations, such as rare event sampling schemes, and the theoretical accuracy level could be improved systematically by going to higher orders in the difference path variables.61,7

Fourth, it is observed here that the numerical error of the FGR rate constant calculation is primarily due to the exponential factor in $\tilde{C}_{AD}(\omega) = e^{\beta\hbar\omega/2}\tilde{G}_{AD}(\omega)$, which causes an error in the deep inverted region. Using a smoothing algorithm, the accuracy of OCPI could be improved significantly, which is attributed to a less noisy short-time region in the symmetrized TCF as a result of the smoothing. Alternatively, numerical issues may be circumvented if the OCPI method can be applied to the Kubo-transformed TCF, 37 which does not contain an unbounded exponential conversion factor.

Fifth, it should be possible to generalize the current OCPI technique of two-state TCFs for general anharmonic and non-Condon systems, ^{57,72,73} correlated multidimensional PESs, ⁶³ and linear and nonlinear spectroscopies ^{39,74,75} described by multi-time multi-state TCFs. ^{39,63} It will be important to extend the OCPI to anharmonic systems, where one could test the OCPI implementation, sampling, and accuracy of the second-order approximation, and we will report a comprehensive study on the anharmonic models in a future work. In condensed-phase systems, the quantum coherence reflected in the symmetrized TCF is expected to lead to fast decay of the TCF, which makes it easier to perform an OCPI calculation; however,

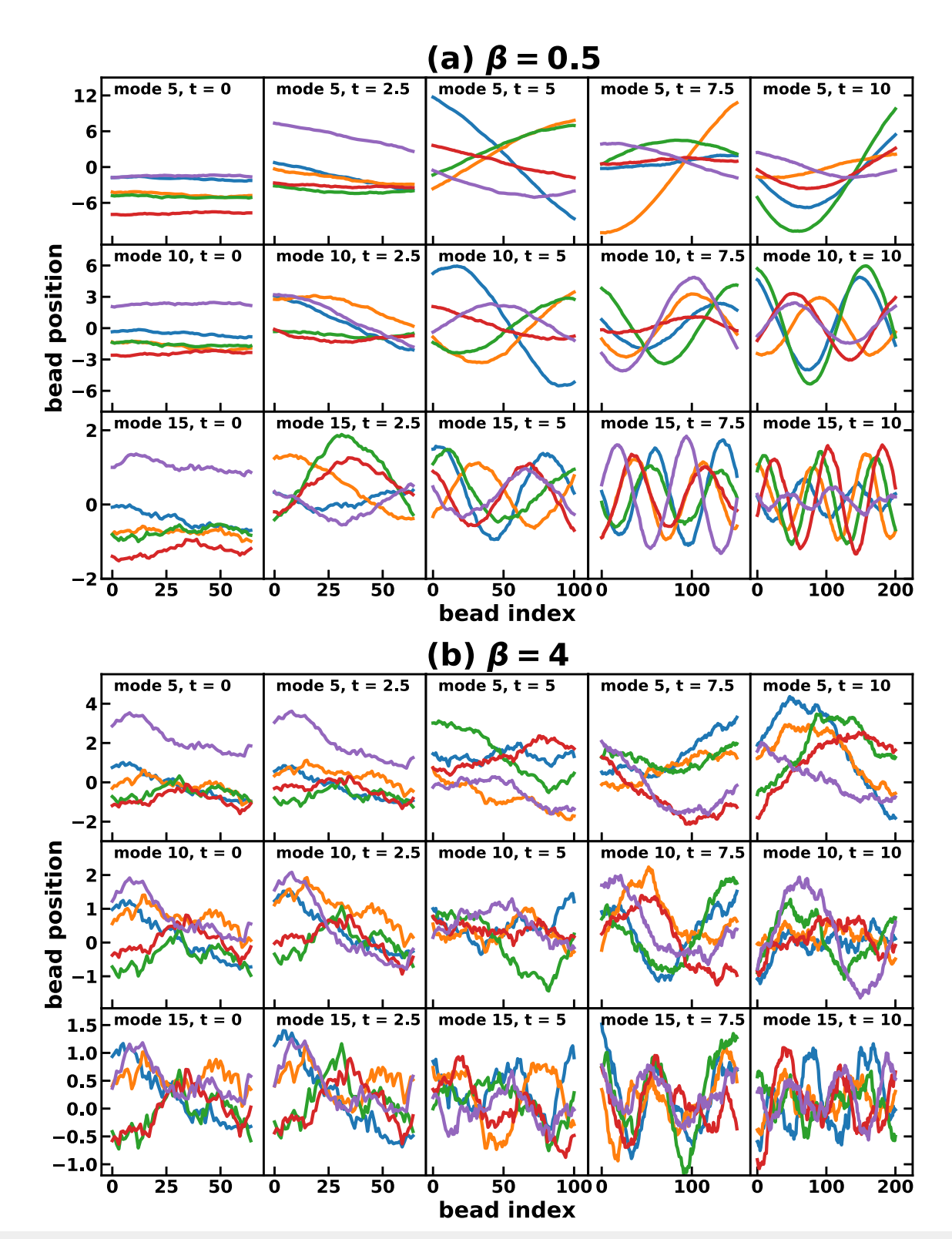


FIG. 8. Snapshots of sampled open chains in the imaginary-time OCPI simulations for representative low, medium, and high frequency modes of the spin-boson model (mode 5, mode 10, and mode 15) for different times (t = 0, 2.5, 5, 7.5, 10) at temperatures (a) $\beta = 0.5$ and (b) $\beta = 4$.

one must still deal with a large number of degrees of freedom. With more complicated TCF forms, it may be nontrivial to formulate the corresponding OCPI theory.

VI. CONCLUDING REMARKS

Quantum time correlation functions that involve multiple electronic states are essential for nonadiabatic quantum dynamics. In this paper, we proposed an imaginary-time open-chain path-integral (OCPI) sampling method for calculating two-state quantum time correlation functions and applied it to calculate the Fermi's golden rule charge transfer rate constant between two electronic states. The OCPI approach directly computes the two-state symmetrized time correlation function, which contains equivalent dynamical information to the standard two-state quantum time correlation function, as seen in Eq. (14). The two-state OCPI formalism expresses the twostate symmetrized TCF, $G_{AD}(t)$, in terms of forward and backward path integrals on the donor and the acceptor PESs. We write the 2P forward and backward path variables in terms of (P + 1) average and (P-1) difference path variables as in LSC/LPI, followed by Taylor expansion of the two electronic PESs up to second order in the difference path variables, allowing us to integrate out the difference variables analytically. As a result, we obtain an effective potential as a function of the open-chain variables of (P+1) beads, which are subject to the average PES between the donor and the acceptor PESs, along with other extended OCPI terms. We propose an imaginary-time OCPI sampling scheme for evaluating $G_{AD}(t)$ that involves complex quantum phase factors originating from electronic quantum coherence.

With the two-state OCPI method developed here, we computed the FGR charge transfer rate constant for a widely used spin-boson model at high and low temperatures. The OCPI calculation was implemented using open path integral molecular dynamics (OPIMD) with a thermostat to sample the open-chain configurations in the effective potential. Results show that OCPI gives an accurate $G_{AD}(t)$, which can be converted to the FGR rate constant $(k = \tilde{C}_{AD}(\omega_{DA})/\hbar^2)$ that agrees well with the analytical results, ranging from the normal regime to the inverted regime. Compared with the real-time LSC/LPI approach and the classic Marcus theory, OCPI together with LSC/LPI was found to offer accurate FGR CT rate constants covering the entire turnover, while the Marcus theory is seen to fail at low temperature or in the deep inverted region. The oscillations of the end-to-end distances of the open chains perfectly match the mode's oscillation period, which suggests that the open-chain beads in order from first to last correspond to physical time zero through final time t. This feature indicates that the "complex-time" OCPI contains real-time information. Ultimately, the OCPI approach brings a new way of formulating the real-time quantum dynamics involving two electronic states using imaginarytime sampling and is shown to be capable of capturing electronic quantum coherence and nuclear quantum effect accurately. It will be important to test this approach in realistic condensed-phase systems such as photoinduced charge transfer in liquid solutions⁵⁷ and interfacial semiconductors.

ACKNOWLEDGEMENT

X.S. acknowledges support from the Hefei National Laboratory for Physical Sciences at the Microscale (Grant No. KF2020008),

the National Natural Science Foundation of China (Grant No. 21903054), and the Program for Eastern Young Scholar at Shanghai Institutions of Higher Learning. Computing resources were provided by NYU Shanghai HPC. M.E.T. acknowledges support from the US National Science Foundation (Grant No. CHE-1955381).

AUTHOR DECLARATIONS

Conflict of Interest

The authors have no conflicts to disclose.

Author Contributions

Zengkui Liu: Data curation (equal); Software (equal); Writing – original draft (equal). Wen Xu: Software (equal). Mark E. Tuckerman: Conceptualization (equal); Funding acquisition (equal); Writing – review & editing (equal). Xiang Sun: Conceptualization (equal); Funding acquisition (equal); Project administration (equal); Supervision (equal); Writing – review & editing (equal).

DATA AVAILABILITY

The data that support the findings of this study are available from the corresponding author upon reasonable request.

APPENDIX: PROOF OF THE RELATION BETWEEN THE TWO-STATE SYMMETRIZED TCF AND THE STANDARD TCF [Eq. (14)]

Here, we derive the relation between the standard quantum TCF $C_{AD}(t)$ and the symmetrized TCF $G_{AD}(t)$ as in Eq. (14). First, we expand $C_{AD}(t)$ and $G_{AD}(t)$ in the energy basis of the donor and acceptor Hamiltonians, i.e., $\hat{H}_D|j^D\rangle = E_j^D|j^D\rangle$ and $\hat{H}_A|j^A\rangle = E_j^A|j^A\rangle$,

$$\begin{split} C_{AD}(t) &= \frac{1}{Z_D} \operatorname{Tr} \Big[e^{-\beta \hat{H}_D} \hat{A} e^{i\hat{H}_A t/\hbar} \hat{B} e^{-i\hat{H}_D t/\hbar} \Big] \\ &= \frac{1}{Z_D} \sum_{j,k} \operatorname{Tr} \Big[e^{-\beta \hat{H}_D} \big| j^D \big\rangle \langle j^D \big| \hat{A} \big| k^A \big\rangle \langle k^A \big| e^{i\hat{H}_A t/\hbar} \hat{B} e^{-i\hat{H}_D t/\hbar} \Big] \\ &= \frac{1}{Z_D} \sum_{j,k} e^{-\beta E_j^D} A_{jk}^{DA} B_{kj}^{AD} e^{i\omega_{kj}^{AD} t}, \end{split} \tag{A1}$$

where $A_{jk}^{DA}=\langle j^D|\hat{A}|k^A\rangle$, $B_{kj}^{AD}=\langle k^A|\hat{B}|j^D\rangle$, and $\hbar\omega_{kj}^{AD}=E_k^A-E_j^D$. Taking Fourier transform of $C_{AD}(t)$, we have

$$\tilde{C}_{AD}(\omega) = \frac{2\pi}{Z_D} \sum_{i,k} e^{-\beta E_j^D} A_{jk}^{DA} B_{kj}^{AD} \delta(\omega_{kj}^{AD} - \omega). \tag{A2}$$

Next, we expand $G_{AD}(t)$ in the energy basis,

$$G_{AD}(t) = \frac{1}{Z_D} \operatorname{Tr} \left[\hat{A} e^{i\hat{H}_A \tau_{\epsilon}^*/\hbar} \hat{B} e^{-i\hat{H}_D \tau_{\epsilon}/\hbar} \right]$$

$$= \frac{1}{Z_D} \sum_{j,k} \operatorname{Tr} \left[|j^D\rangle \langle j^D| \hat{A} e^{i\hat{H}_A \tau_{\epsilon}^*/\hbar} |k^A\rangle \langle k^A| \hat{B} e^{-i\hat{H}_D \tau_{\epsilon}^*/\hbar} \right]$$

$$= \frac{1}{Z_D} \sum_{j,k} A_{jk}^{DA} B_{kj}^{AD} e^{i\omega_{kj}^{AD} t/\hbar} e^{-\beta (E_j^D + E_k^A)/2}. \tag{A3}$$

Taking Fourier transform of $G_{AD}(t)$, we have

$$\tilde{G}_{AD}(\omega) = \frac{2\pi}{Z_D} \sum_{i,k} A^{DA}_{jk} B^{AD}_{kj} \delta(\omega^{AD}_{kj} - \omega) e^{-\beta E^D_j} e^{-\beta\hbar\omega/2}.$$
 (A4)

Comparing Eqs. (A2) and (A4), we obtain the relationship

$$\tilde{C}_{AD}(\omega) = e^{\beta\hbar\omega/2}\tilde{G}_{AD}(\omega).$$
 (A5)

REFERENCES

- ¹B. J. Berne and G. D. Harp, "On the calculation of time correlation functions," Adv. Chem. Phys. 17, 63–227 (1970).
- ²M. E. Tuckerman, D. Marx, M. L. Klein, and M. Parrinello, "On the quantum nature of the shared proton in hydrogen bonds," Science 275, 817–820 (1997).
- ³T. E. Markland and M. Ceriotti, "Nuclear quantum effects enter the mainstream," Nat. Rev. Chem. **2**, 0109 (2018).
- ⁴J. Z. H. Zhang, *Theory and Application of Quantum Molecular Dynamics* (World Scientific, Singapore, 1999).
- ⁵N. Makri and W. H. Miller, "Time-dependent self-consistent field (TDSCF) approximation for a reaction coordinate coupled to a harmonic bath: Single and multiple configuration treatments," J. Chem. Phys. **87**, 5781–5787 (1987).
- ⁶M. H. Beck, A. Jäckle, G. A. Worth, and H. D. Meyer, "The multiconfiguration time-dependent Hartree (MCTDH) method: A highly efficient algorithm for propagating wavepackets," Phys. Rep. 324, 1–105 (2000).
 ⁷S. M. Greene and V. S. Batista, "Tensor-train split-operator Fourier trans-
- ⁷S. M. Greene and V. S. Batista, "Tensor-train split-operator Fourier transform (TT-SOFT) method: Multidimensional nonadiabatic quantum dynamics," J. Chem. Theory Comput. 13, 4034–4042 (2017).
- ⁸X. Sun and W. H. Miller, "Semiclassical initial value representation for electronically nonadiabatic molecular dynamics," J. Chem. Phys. **106**, 6346–6353 (1997).
- ⁹X. Sun and W. H. Miller, "Mixed semiclassical-classical approaches to the dynamics of complex molecular systems," J. Chem. Phys. **106**, 916–927 (1997).
- ¹⁰W. H. Miller, "The semiclassical initial value representation: A potentially practical way for adding quantum effects to classical molecular dynamics simulations," J. Phys. Chem. A 105, 2942–2955 (2001).
- ¹¹ N. Makri and K. Thompson, "Semiclassical influence functionals for quantum systems in anharmonic environments," Chem. Phys. Lett. 291, 101–109 (1998).
- ¹²K. Thompson and N. Makri, "Influence functionals with semiclassical propagators in combined forward-backward time," J. Chem. Phys. 110, 1343–1353 (1999).
- ¹³K. Thompson and N. Makri, "Rigorous forward-backward semiclassical formulation of many-body dynamics," Phys. Rev. E **59**, 4729–4732 (1999).
- ¹⁴H. Wang, X. Sun, and W. H. Miller, "Semiclassical approximations for the calculation of thermal rate constants for chemical reactions in complex molecular systems," J. Chem. Phys. 108, 9726–9736 (1998).
- ¹⁵X. Sun, H. Wang, and W. H. Miller, "Semiclassical theory of electronically nonadiabatic dynamics: Results of a linearized approximation to the initial value representation," J. Chem. Phys. **109**, 7064–7074 (1998).
- ¹⁶J. Liu and W. H. Miller, "A simple model for the treatment of imaginary frequencies in chemical reaction rates and molecular liquids," J. Chem. Phys. 131, 074113 (2009).
- ¹⁷K. İmre, E. Özizmir, M. Rosenbaum, and P. F. Zweifel, "Wigner method in quantum statistical mechanics," J. Math. Phys. 8, 1097–1108 (1967).
- ¹⁸Q. Shi and E. Geva, "Semiclassical theory of vibrational energy relaxation in the condensed phase," J. Phys. Chem. A 107, 9059–9069 (2003).
- ¹⁹Q. Shi and E. Geva, "Vibrational energy relaxation in liquid oxygen from a semiclassical molecular dynamics simulation," J. Phys. Chem. A **107**, 9070–9078 (2003).
- ²⁰Q. Shi and E. Geva, "Nonradiative electronic relaxation rate constants from approximations based on linearizing the path-integral forward-backward action," J. Phys. Chem. A 108, 6109–6116 (2004).

- ²¹ J. A. Poulsen, G. Nyman, and P. J. Rossky, "Practical evaluation of condensed phase quantum correlation functions: A Feynman–Kleinert variational linearized path integral method," J. Chem. Phys. 119, 12179–12193 (2003).
- ²²J. A. Poulsen, G. Nyman, and P. J. Rossky, "Quantum diffusion in liquid para-hydrogen: An application of the Feynman-Kleinert linearized path integral approximation," J. Phys. Chem. B 108, 19799–19808 (2004).
 ²³J. A. Poulsen, G. Nyman, and P. J. Rossky, "Determination of the Van Hove
- ²³ J. A. Poulsen, G. Nyman, and P. J. Rossky, "Determination of the Van Hove spectrum of liquid He(4): An application of the Feynman–Kleinert linearized path integral methodology," J. Phys. Chem. A **108**, 8743–8751 (2004).
- ²⁴S. Bonella and D. Coker, "Linearized, time-dependent, non-adiabatic quantum correlation functions," Comput. Phys. Commun. 169, 267–273 (2005).
- ²⁵S. Bonella, D. Montemayor, and D. F. Coker, "Linearized path integral approach for calculating nonadiabatic time correlation functions," Proc. Natl. Acad. Sci. U. S. A. 102, 6715–6719 (2005).
- ²⁶R. P. Feynman, "Space-time approach to non-relativistic quantum mechanics," Rev. Mod. Phys. **20**, 367–387 (1948).
- ²⁷R. P. Feynman and H. Kleinert, "Effective classical partition functions," Phys. Rev. A 34, 5080-5084 (1986).
- ²⁸B. J. Berne and D. Thirumalai, "On the simulation of quantum systems: Path integral methods," Annu. Rev. Phys. Chem. **37**, 401–424 (1986).
- ²⁹M. E. Tuckerman, Statistical Mechanics: Theory and Molecular Simulation (Oxford University Press, New York, 2010).
- ³⁰D. Chandler and P. G. Wolynes, "Exploiting the isomorphism between quantum theory and classical statistical mechanics of polyatomic fluids," J. Chem. Phys. **74**, 4078–4095 (1981).
- ³¹ D. M. Ceperley, "Path integrals in the theory of condensed helium," Rev. Mod. Phys. **67**, 279–355 (1995).
- 32 M. Parrinello and A. Rahman, "Study of an F center in molten KCl," J. Chem. Phys. 80, 860-867 (1984).
- ³³ M. E. Tuckerman, B. J. Berne, G. J. Martyna, and M. L. Klein, "Efficient molecular dynamics and hybrid Monte Carlo algorithms for path integrals," J. Chem. Phys. 99, 2796–2808 (1993).
- ³⁴D. Marx and M. Parrinello, "*Ab initio* path integral molecular dynamics: Basic ideas," J. Chem. Phys. **104**, 4077–4082 (1996).
- ³⁵B. Hirshberg, V. Rizzi, and M. Parrinello, "Path integral molecular dynamics for bosons," Proc. Natl. Acad. Sci. U. S. A. 116, 21445–21449 (2019).
- ³⁶J. Cao and G. A. Voth, "The formulation of quantum statistical mechanics based on the Feynman path centroid density. IV. Algorithms for centroid molecular dynamics," J. Chem. Phys. **101**, 6168–6183 (1994).
- ³⁷I. R. Craig and D. E. Manolopoulos, "Quantum statistics and classical mechanics: Real time correlation functions from ring polymer molecular dynamics," J. Chem. Phys. **121**, 3368–3373 (2004).
- ³⁸T. J. H. Hele, M. J. Willatt, A. Muolo, and S. C. Althorpe, "Boltzmann-conserving classical dynamics in quantum time-correlation functions: 'Matsubara dynamics,'" J. Chem. Phys. **142**, 134103 (2015).
- ³⁹Z. Tong, P. E. Videla, K. A. Jung, V. S. Batista, and X. Sun, "Two-dimensional Raman spectroscopy of Lennard-Jones liquids via ring-polymer molecular dynamics," J. Chem. Phys. **153**, 034117 (2020).
- ⁴⁰C. Robertson and S. Habershon, "Harmonic-phase path-integral approximation of thermal quantum correlation functions," J. Chem. Phys. 148, 102316 (2018).
- ⁴¹J. R. Cendagorta, Z. Bačić, and M. E. Tuckerman, "An open-chain imaginary-time path-integral sampling approach to the calculation of approximate symmetrized quantum time correlation functions," J. Chem. Phys. **148**, 102340 (2018).
- ⁴²G. Krilov, E. Sim, and B. J. Berne, "Quantum time correlation functions from complex time Monte Carlo simulations: A maximum entropy approach," J. Chem. Phys. **114**, 1075–1088 (2001).
- ⁴³S. Bonella, M. Monteferrante, C. Pierleoni, and G. Ciccotti, "Path integral based calculations of symmetrized time correlation functions. I," J. Chem. Phys. 133, 164104 (2010).
- ⁴⁴S. Bonella, M. Monteferrante, C. Pierleoni, and G. Ciccotti, "Path integral based calculations of symmetrized time correlation functions. II," J. Chem. Phys. 133, 164105 (2010).
- ⁴⁵J. R. Cendagorta, H. Shen, Z. Bačić, and M. E. Tuckerman, "Enhanced sampling path integral methods using neural network potential energy surfaces with

- application to diffusion in hydrogen hydrates," Adv. Theory Simul. 4, 2000258 (2021).
- ⁴⁶X. Sun and E. Geva, "Equilibrium Fermi's golden rule charge transfer rate constants in the condensed phase: The linearized semiclassical method vs classical Marcus theory," J. Phys. Chem. A **120**, 2976–2990 (2016).
- ⁴⁷X. Sun and E. Geva, "Non-condon equilibrium Fermi's golden rule electronic transition rate constants via the linearized semiclassical method," J. Chem. Phys. 144, 244105 (2016).
- ⁴⁸J. C. Tully, "Molecular dynamics with electronic transitions," J. Chem. Phys. 93, 1061 (1990).
- ⁴⁹P. Ehrenfest, "Comment on the approximate validity of classical mechanics within quantum mechanics," Z. Phys. 45, 455–457 (1927).
- ⁵⁰U. Weiss, *Quantum Dissipative Systems* (World Scientific, Singapore, 2012).
- ⁵¹ D. Xu and K. Schulten, "Coupling of protein motion to electron transfer in a photosynthetic reaction center: Investigating the low temperature behavior in the framework of the spin-boson model," Chem. Phys. 182, 91–117 (1994).
- ⁵²Z. Tong, X. Gao, M. S. Cheung, B. D. Dunietz, E. Geva, and X. Sun, "Charge transfer rate constants for the carotenoid-porphyrin-C₆₀ molecular triad dissolved in tetrahydrofuran: The spin-boson model vs the linearized semiclassical approximation," J. Chem. Phys. 153, 044105 (2020).
- ⁵³A. Nitzan, Chemical Dynamics in Condensed Phases: Relaxation, Transfer and Reactions in Condensed Molecular Systems (Oxford University Press, New York, 2006).
- ⁵⁴R. D. Coalson, D. G. Evans, and A. Nitzan, "A nonequilibrium golden rule formula for electronic state populations in nonadiabatically coupled systems," J. Chem. Phys. **101**, 436 (1994).
- 55 X. Sun and E. Geva, "Nonequilibrium Fermi's golden rule charge transfer rates via the linearized semiclassical method," J. Chem. Theory Comput. 12, 2926–2941 (2016).
- ⁵⁶X. Sun and E. Geva, "Non-condon nonequilibrium Fermi's golden rule rates from the linearized semiclassical method," J. Chem. Phys. 145, 064109 (2016).
- 57 Z. Hu, Z. Tong, M. S. Cheung, B. D. Dunietz, E. Geva, and X. Sun, "Photoinduced charge transfer dynamics in the carotenoid–porphyrin– C_{60} triad via the linearized semiclassical nonequilibrium Fermi's golden rule," J. Phys. Chem. B **124**, 9579–9591 (2020).
- ⁵⁸D. M. Ceperley and E. L. Pollock, "Path-integral computation of the low-temperature properties of liquid ⁴He," Phys. Rev. Lett. **56**, 351–354 (1986).
- ⁵⁹J. A. Morrone, V. Srinivasan, D. Sebastiani, and R. Car, "Proton momentum distribution in water: An open path integral molecular dynamics study," J. Chem. Phys. 126, 234504 (2007).
- 60 D. Weingarten, "Complex probabilities on \mathbb{R}^N as real probabilities on \mathbb{C}^N and an application to path integrals," Phys. Rev. Lett. **89**, 240201 (2002).
- ⁶¹ A. Pérez and M. E. Tuckerman, "Improving the convergence of closed and open path integral molecular dynamics via higher order Trotter factorization schemes," J. Chem. Phys. 135, 064104 (2011).
- ⁶²P. L. Walters, T. C. Allen, and N. Makri, "Direct determination of discrete harmonic bath parameters from molecular dynamics simulations," J. Comput. Chem. 38, 110–115 (2017).

- ⁶³ Z. Hu, D. Brian, and X. Sun, "Multi-state harmonic models with globally shared bath for nonadiabatic dynamics in the condensed phase," J. Chem. Phys. 155, 124105 (2021).
- ⁶⁴H. Wang, "Iterative calculation of energy eigenstates employing the multi-layer multiconfiguration time-dependent Hartree theory," J. Phys. Chem. A 118, 9253–9261 (2014).
- ⁶⁵M. Ceriotti, M. Parrinello, T. E. Markland, and D. E. Manolopoulos, "Efficient stochastic thermostatting of path integral molecular dynamics," J. Chem. Phys. **133**, 124104 (2010).
- ⁶⁶P. H. C. Eilers, "A perfect smoother," Anal. Chem. 75, 3631–3636 (2003).
- ⁶⁷J. Midelet, A. H. El-Sagheer, T. Brown, A. G. Kanaras, A. Débarre, and M. H. V. Werts, "Spectroscopic and hydrodynamic characterisation of DNA-linked gold nanoparticle dimers in solution using two-photon photoluminescence," ChemPhysChem 19, 827–836 (2018).
- ⁶⁸B. Szekeres, L. B. Pártay, and E. Mátyus, "Direct computation of the quantum partition function by path-integral nested sampling," J. Chem. Theory Comput. 14, 4353–4359 (2018).
- ⁶⁹ J. Liu and W. H. Miller, "Linearized semiclassical initial value time correlation functions using the thermal Gaussian approximation: Applications to condensed phase systems," J. Chem. Phys. **127**, 114506 (2007).
- ⁷⁰ J. A. Poulsen and G. Nyman, "A divergence-free wigner transform of the Boltzmann operator based on an effective frequency theory," J. Phys. Chem. A 125, 9209–9225 (2021).
- ⁷¹ V. Kapil, J. Behler, and M. Ceriotti, "High order path integrals made easy," J. Chem. Phys. 145, 234103 (2016).
- ⁷²X. Sun, P. Zhang, Y. Lai, K. L. Williams, M. S. Cheung, B. D. Dunietz, and E. Geva, "Computational study of charge-transfer dynamics in the carotenoid–porphyrin–C₆₀ molecular triad solvated in explicit tetrahydrofuran and its spectroscopic signature," J. Phys. Chem. C 122, 11288–11299 (2018).
- ⁷³D. Brian and X. Sun, "Linear-response and nonlinear-response formulations of the instantaneous Marcus theory for nonequilibrium photoinduced charge transfer," J. Chem. Theory Comput. 17, 2065–2079 (2021).
- ⁷⁴S. Karsten, S. I. Bokarev, S. G. Aziz, S. D. Ivanov, and O. Kühn, "A time-correlation function approach to nuclear dynamical effects in X-ray spectroscopy," J. Chem. Phys. **146**, 224203 (2017).
- ⁷⁵ X. Gao and E. Geva, "A nonperturbative methodology for simulating multidimensional spectra of multiexcitonic molecular systems via quasiclassical mapping Hamiltonian methods," J. Chem. Theory Comput. 16, 6491–6502 (2020).
- ⁷⁶D. Brian and X. Sun, "Charge-transfer landscape manifesting the structure-rate relationship in the condensed phase via machine learning," J. Phys. Chem. B 125, 13267–13278 (2021).
- ⁷⁷J. Tinnin, S. Bhandari, P. Zhang, E. Geva, B. D. Dunietz, X. Sun, and M. S. Cheung, "Correlating interfacial charge transfer rates with interfacial molecular structure in the tetraphenyldibenzoperiflanthene/ C_{70} organic photovoltaic system," J. Phys. Chem. Lett. 13, 763–769 (2022).